Dynamic Identification of Steel Truss Structures and Parametric Inference Using Optimally Placed Strain Gauges

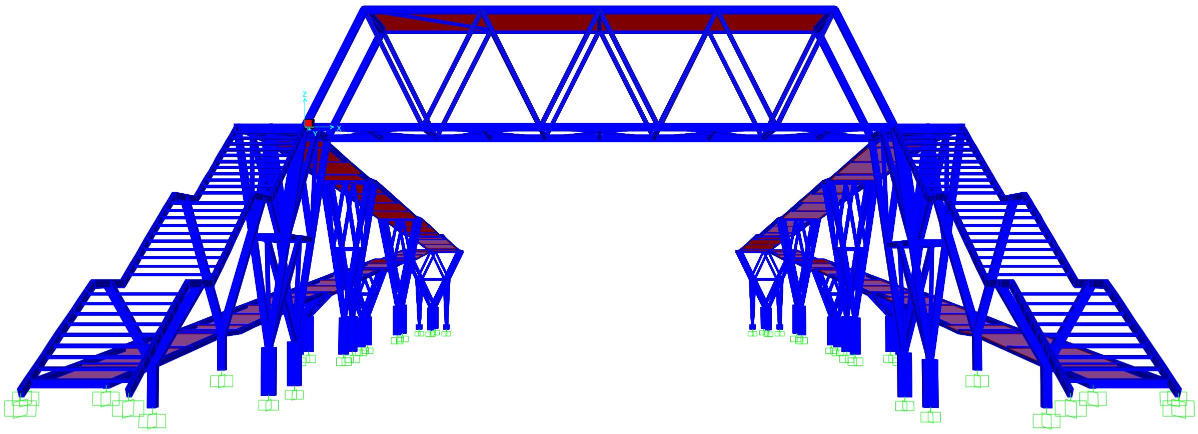

Trabajo de Fin de Máster Defendido por:

Antonio Luis Sánchez López-Cuervo

Bajo la Cotutorización de:

Dr. Enrique García Macías
Dr. Juan Chiachío Ruano

Máster Universitario en Estructuras

Curso 2023-2024

Convocatoria Ordinaria de Septiembre

Título

Identificación Dinámica de Estructuras de Acero e Inferencia Paramétrica Usando Galgas Extensiométricas con Localización Optimizada.

Autor

Antonio Luis Sánchez López-Cuervo

Palabras Clave

Análisis Modal Operacional, Galgas Extensiométricas, Independencia Efectiva, Monitorización Basada en Vibraciones, Monitorización de la Salud Estructural, Posicionamiento Óptimo de Sensores,

Resumen

Las infraestructuras civiles son vitales para el desarrollo de las sociedades: impulsan el crecimiento económico, reducen la pobreza y mejoran la calidad de vida de los ciudadanos. Es por ello que evitar el deterioro debido a la exposición a factores medioambientales, el incremento en cargas de uso y los sucesos extremos, supone un auténtico reto político y social. Un mantenimiento eficaz es crucial para garantizar la seguridad, la capacidad de servicio y la durabilidad de estas estructuras, por lo que la monitorización de la salud estructural tá cobrando cada vez más importancia. Entre las técnicas de monitorización de salud estructural, una de las más ampliamente utilizadas es el seguimiento de los parámetros modales obtenidos mediante la monitorización de vibraciones con acelerómetros. Sin embargo, estos sensores presentan ciertas limitaciones, como la alta sensibilidad a las condiciones climáticas.

El presente TFM explora el análisis modal de deformaciones como alternativa a la monitorización de vibraciones basada en acelerómetros. El estudio se centra en la optimización de la colocación de las galgas extensiométricas mediante el uso del algoritmo de Independencia Efectiva (IE). El objetivo principal de esta investigación es validar dicho algoritmo en estructuras reales a través de dos casos de estudio: una estructura de laboratorio y una pasarela peatonal real. La metodología implica el desarrollo de Modelos de Elementos Finitos (MEFs) en *SAP2000*, la implementación del algoritmo de IE en Python y la aplicación del análisis modal operacional (OMA) en ambas estructuras. El estudio también incorpora la inferencia bayesiana mediante el método de Monte Carlo Markov Chain para actualizar el MEF de la estructura de laboratorio basándose en los parámetros modales identificados mediante el Análisis Modal Operacional.

Los resultados demuestran la aplicabilidad de galgas extensiométricas en la realización de análisis modal operacional en deformaciones, y la eficacia del algoritmo de IE para la colocación óptima de estos sensores, proporcionando valiosos conocimientos para la aplicación práctica de sistemas monitorización de la salud estructural en infraestructuras del mundo real.

Title

Dynamic Identification of Steel Truss Structures and Parametric Inference Using Optimally Placed Strain Gauges.

Author

Antonio Luis Sánchez López-Cuervo

Key Words

Effective Independence (EfI), Operational Modal Analysis (OMA), Optimal Sensor Placement (OSP), Strain Gauges (SGs), Structural Health Monitoring (SHM), Vibration-Based Monitroing (VBM).

Abstract

Infrastructure is vital for societal development, driving economic growth, reducing poverty, and enhancing quality of life. However, infrastructure faces challenges such as deterioration and damage due to environmental factors, operational loads, and extreme events. Effective maintenance is crucial for ensuring the safety, serviceability, and durability of these structures, making Structural Health Monitoring (SHM) increasingly important. Among SHM techniques, Vibration-Based Monitoring (VBM) is widely used, traditionally employing accelerometers to assess modal properties. However, these sensors have certain limitations, such as reduced sensitivity to local defects.

This Master Thesis explores strain modal analysis as an alternative to accelerometers-based VBM. The study focuses on optimizing the placement of Strain Gauges (SGs) by the use of the Effective Independence (EfI) algorithm. The primary objective of this research is to validate the EfI method in real structures through two case studies: a laboratory steel frame and an in-operation pedestrian footbridge. The methodology involves the development of Finite Element Models (FEMs) in *SAP2000*, the implementation of the EfI method in Python, and the application of Operational Modal Analysis (OMA) on both structures. The study also incorporates Bayesian Inference using the Markov Chain Monte Carlo (MCMC) method to update the steel frame FEM based on modal parameters identified by OMA.

The results demonstrate the applicability of SGs in conducting deformation-based OMA and the effectiveness of the EfI algorithm for the optimal placement of these sensors. These findings offer valuable insights for the practical application of SHM systems in real-world infrastructure.

Acknowledgment

First and foremost, I would like to express my deepest gratitude to my thesis supervisors:

Professor Juan Chiachío Ruano, for his continuous support and encouragement to pursue a PhD, as well as for providing me with the necessary resources to ensure the highest quality in the research undertaken. I am especially thankful for the financial support for the acquisition of the SGs and PCBs used in this work, without which this project would not have been possible. I am also grateful for the materials and guidance provided for my training in Bayesian Inference.

Professor Enrique García Macías, for his exceptional dedication and supervision of this dissertation. I am very grateful for his guidance and for addressing all the questions that arose throughout this process, from the assembly of the steel frame to algorithms implementation. The results obtained in this thesis will serve as the foundation for my first scientific publication, which would not have been achievable without his invaluable support.

I would also like to extend my heartfelt thanks to Alba and my family, for their unwavering support and for always encouraging me to pursue my professional goals.

Contents

List of Figures

List of Tables

List of Algorithms

Acronyms

- CAGR: Compound Annual Growth Rate
- COV-SSI: Covariance-Driven Stochastic Subspace Identification
- CPSD: Cross Power Spectral Density
- DC: Direct Current
- DOF: Degree of Freedom
- EFDD: Enhanced Frequency Domain Decomposition
- EfI: Effective Independence
- FBG: Fiber Bragg Grating
- FDD: Frequency Domain Decomposition
- FEM: Finite Element Model
- FIM: Fisher Information Matrix
- FRF: Frequency Response Function
- IE: Independencia Efectiva
- IFT: Inverse Fourier Transform
- MAC: Modal Assurance Criterion
- MCMC: Markov Chain Monte Carlo
- MDOF: Multiple Degree of Freedom
- MEF: Modelo de Elementos Finitos
- MH: Metropolis Hastings
- OAPI: Open Application Programming Interface
- ODE: Ordinary Differential Equation
- OMA: Operational Modal Analysis
- OSP: Optimal Sensor Placement

- PCB: Printed Circuit Board
- PDF: Probability Density Function
- PME: Principle of Maximum Entropy
- SFRF: Strain Frequency Response Function
- SG: Strain Gauge
- SHM: Structural Health Monitoring
- SVD: Singular Value Decomposition
- SVP: Singular Value Plot
- VBM: Vibration-Based Monitoring

Chapter 1

Motivation, Objectives and Methodology

1.1. Motivation

Infrastructure plays an essential role in society, serving as a key driver for reducing poverty, promoting economic growth, improving social cohesion, and enhancing the quality of life and well-being [1–3]. This importance is reflected in the significant investments that public institutions make in constructing and maintaining civil infrastructure. For example, the average EU investment in infrastructure in recent years exceeds 1.5% of GDP [4], representing only a portion of the total investments made in buildings and other structures.

However, as infrastructure ages, deterioration and damage might appear due to exposure to environmental and operational loads, faulty design, construction errors or extreme events such as earthquakes [5]. In the US, 7.5% of the nation's bridges are considered structurally deficient, meaning they are in "poor" condition [6]. In Europe, many road bridges over 100 m in the major European transport corridors of the Trans-European Transport Network (TEN-T) are carrying significantly larger loads than they were originally designed for, and many of these structures are reaching the end of their expected lifespan [7].

To prevent deterioration and ensure safety, serviceability, and durability, preventive maintenance emerges as the most cost-effective strategy. Reference [8] provides different examples supporting this approach. For instance, in the case of roads, it was found that returns on maintenance were almost twice as much as those on projects involving mainly new construction. This trend was even more pronounced in Latin America, where every $1 not spent on maintenance is estimated to result in $3 to $4 in premature reconstruction [8]. The disparity is even greater for power lines, where the expenditure of $1 million to reduce power line losses could save $12 million in generating capacity [8].

Reflecting the growing emphasis on maintenance, the markets for Structural Health Monitoring (SHM) and related technologies are expanding rapidly. For example, the European SHM market is forecasted to grow at a Compound Annual Growth Rate (CAGR) of 16.3% by 2030 [9]. A similar trend is observed in the US, where the SHM market is expected to grow at a CAGR of 18.8% by 2030 [10]. Regarding digital twins for buildings, its global market is projected to grow at a CAGR of 32.6% from 2024 to 2032 [11].

One of the most widely used techniques for guiding maintenance is Vibration-Based Monitoring (VBM). VBM is a non-destructive method that identifies a system's modal properties (natural frequencies, damping rates and mode shapes) to assess its condition state and identify damage. Traditionally, VBM is performed using accelerometers, but this approach has well-known limitations to identify local defects with reduced impact on the overall stiffness of structures [12–14].

Alternatively, the strain modal analysis is a promising VBM technique due to its high sensitivity to local damage [15–17]. It can be performed with SGs, that are cost-effective and easy to install sensors that measure strain at the point in which they are located.

For strain modal analysis to be fully cost-effective, it is important to avoid redundant information, ease data management, and minimize costs. Optimal Sensor Placement (OSP) is defined as the placement of sensors that results in the least amount of monitoring cost while meeting predefined performance requirements [18]. OSP for strain modal analysis has not been fully covered in the literature and is of significant interest for its potential to enhance the efficiency of strain-based VBM.

1.2. Objectives

The primary objective of this work is to demonstrate the effectiveness of the Effective Independence (EfI) method for parameter identification in real structures. This main objective is structured around the following sub-objectives:

O1 Validate the use of conventional SGs and low-cost electronic equipment for conducting strain-based OMA.

O2 Compare the linear independence of extracted mode shapes using optimally and sub-optimally (following purely engineering criteria) placed SGs.

O3 Employ strain modal properties for parameter inference through a Bayesian Approach.

1.3. Methodology

The methodology of the project is articulated around the following key steps:

- Literature review of strain modal analysis and OSP techniques for strain sensors, with special focus on the EfI method.
- Development of a Finite Element Model (FEM) in *SAP2000* for two cases of study: a laboratory steel frame and a real-world steel footbridge.
- Implementation of the EfI method in Python with the use of *SAP2000 Open Application Programming Interface (OAPI)*, to determine the OSP of SGs in both structures.
- Perform OMA on both case studies using optimal and sub-optimal sensor configurations. For the steel footbridge, output data is simulated, as the real monitoring campaign is scheduled for September.
- Implementation of the Markov Chain Monte Carlo (MCMC) method in Python to perform model updating through Bayesian Inference in the laboratory steel frame.

1.4. State of the Art

1.4.1. Strain Modal Analysis

Damage is defined as any significant factor influencing the structural behaviour in such a way that leads to degradation in the current or future performance of a structure [19]. VBM detects and localizes damage by analyzing its effects on the modal properties of the structure, such as frequencies, mode shapes, and damping ratios. OMA enables the identification of the modal parameters by only measuring the output response of the monitored structure without knowing the input excitation forces. When OMA is performed in civil engineering structures, accelerometers are commonly used [20]. On this basis, the modal parameters, namely natural frequencies, (displacement) mode shapes and damping ratios, are estimated from the ambient vibration response of the structure.

One of the main challenges for VBM based on accelerometers is to identify characteristics that are sensitive to damage yet unaffected by environmental factors [20–22]. Natural frequencies, in particular, are not immune to such influences: they can vary by 2-3% due to daily changes in temperature [17, 23] and even more significantly in some cases[1]. The impact of local damage on natural frequencies can be so minimal that it might be completely masked by the frequency variability, as seen in [24]. Consequently, natural frequencies are generally only effective in identifying moderate or severe damage, as demonstrated in [13].

Displacement mode shapes have the advantage of being much less dependent on weather conditions [25], being more effective for damage localization (e.g. through its effect on modal curvature [15]). However, this approach requires a dense spatial discretization of the mode shapes with a large number of sensors, as well as some processing of the obtained mode shapes, which can introduce significant errors [20]. In addition, local damage to hyperstatic structures not only causes changes in modal shapes in that area, but also outside it, which makes it difficult to localise the damage.

As an alternative, strain modal analysis can be performed to obtain both vibration frequencies and strain mode shapes. One key advantage of strain mode shapes is the fact that they are insensitive to temperature effects, as demonstrated in different experiences in both laboratory and real civil engineering structures [16, 17, 24]. Additionally, strain mode shapes are highly sensitive to local damage, making them effective for damage localization, as demonstrated in [24]. Furthermore, related strain modal properties more suited for damage localization, such as modal curvatures, can be directly obtained by strategically locating the strain sensors (e.g. on the upper and lower parts of beams), as shown in [26]. This method is significantly more accurate than deriving displacement mode shapes, as discussed in [20].

The most commonly used strain sensor are: Strain Gauges (SGs), Fiber Bragg Grating (FBG) and Distributed Optical Fiber Sensors (DOFS). SGs (see Figure 1.1a) are particularly suitable in situations where size, weight, or sensor placement are key constraints [27]. Some examples of their use in VBM can be found in references [28, 29]. FBG sensors (depicted in Figure 1.1b) are frequently employed when the aforementioned limitations regarding size and placement are not restrictive. These sensors offer quasi-distributed strain information, making them very attractive in civil engineering structures. Some examples of their application can be found in [16, 17, 24]. Additionally, DOFS (see Figure

[1] For instance, variations exceeding 13% were observed for all identified frequencies in [13], due to the effect of temperature on the deck pavement stiffness.

1.1c) are being increasingly adopted due to their capability to provide continuous assessment of strain along the length of the sensor. An example of its application on a real bridge is described in [26].

Other strain sensor technologies, such as piezoelectric strain sensors (see e.g. [27]) and carbon cement-based transducers [30], are also being explored for strain VBM.

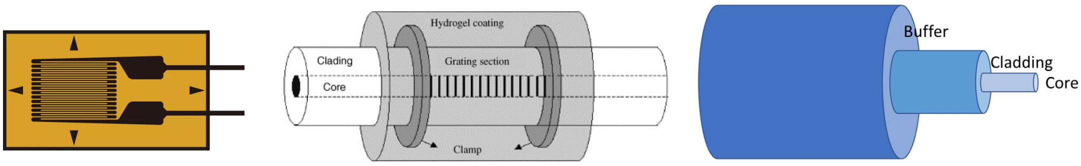

(a) SG (from [31]). (b) FBG (from [32]). (c) DOFS (from [33]).

Figure 1.1: Most commonly used strain sensors in VBM.

1.4.2. Optimal Sensor Placement (OSP)

OSP is defined as the placement of sensors that results in the least amount of monitoring cost while meeting predefined performance requirements [18]. OSP directly decreases the structure life cycle costs, as it reduces the cost related to the instrumentation, the operation, and the maintenance. OSP also reduces indirect costs by improving SHM performance. This improvement leads to a decrease in the risks of false-positive detections, which can cause unnecessary closures, as well as false-negative detections, which might result in unanticipated maintenance costs [34].

In strain monitoring, OSP can address various objectives, such as strain reconstruction for fatigue damage detection, displacement reconstruction, or strain modal analysis for parameter estimation [34]. For fatigue damage detection, OSP aims to position sensors at locations that best reconstruct strain in non-accessible areas. The reconstruction can be achieved using different methods, such as System Equivalent Reduction Expansion Process, Guyan reduction, Inverse Finite Element Method, etc. The accuracy of these reconstructions is often evaluated using metrics such as Mean Square Error and Mean Absolute Error [34].

In strain modal analysis, the OSP problem typically involves determining the minimum number of sensor locations l required to accurately identify the modal parameters for m target modes, out of n possible sensor positions [35] (usually $m \leq l \ll n$). A wide variety of algorithms have been proposed to maximize metrics related to the Modal Kinetic Energy [36], the Singular Value Decomposition Ratio [37], the Fisher Information Matrix (FIM) [38], the Information Entropy [39], among others [40].

Reference [41] used the spectral radius, a lower bound to any norm of the FIM, to maximize the information acquired from strain mode shapes for damage detection. This approach was successfully applied to the FEM of a composite sandwich panel monitored with FBG sensors. Similarly, Zhou et al. [42] developed a two-stage OSP method for optimal displacement reconstruction from strain measurements, applying it to a real antenna for aerospace telecommunications, also monitored with FBG. Cazzulani and co-authors [43] addressed the OSP problem for strain measurements from Distributed Optical Fiber Sensors, applying it to some laboratory structures such as a clamped plate under laboratory conditions [44].

Bayesian approaches have also been employed for OSP. Papadimitriou [45] proposed two algorithms to minimize the information entropy, which is related to the uncertainty in system parameters. In a subsequent work [46], an OSP framework was developed to tackle both strain estimation for fatigue damage detection and strain modal analysis for parameter inference. Their approach for parameter estimation minimized the information entropy by maximizing the determinant of the FIM matrix, which was found to be equivalent to maximizing the expected information gain used for strain estimation. That framework was applied to the FEM of an offshore wind turbine. Additionally, Zhang and co-authors [47] addressed OSP for strain reconstruction using a Bayesian approach that considered strain energy. The method was applied to a full scale beam excited by an hydraulic actuator.

Among the various methodologies, the EfI method [38], aiming to maximize the determinant of the FIM, remains one of the most widely adopted strategies [34]. Originally developed for acceleration, velocity or displacement outputs, the EfI method can also be easily adapted for strain measurements [34]. For example, Kyung and Eun [48] used the EfI method for strain mode shapes and applied it to the FEM of a truss structure. In that work, the advantages of using SGs compared with displacement transducers were highlighted. The EfI formulation has also been extended for using different types of sensors along with strain sensors. Zhang and colleagues [49] extended the EfI method to simultaneously consider displacement transducers and SGs, applying the method to the FEM of a cantilever beam subjected to random forces. Additionally, Zhu et al. [50] expanded the EfI method to include accelerometers, accommodating three types of sensors. The OSP goal in that study was to minimize the overall reconstruction error variance at the locations of interest and ensure that reconstruction errors remained within a desired target level. The method was tested on a simply supported steel beam. In another advancement, Liu et al. [51] introduced a metric called Distance Coefficient to enhance the EfI algorithm in a two-stage optimization framework for response reconstruction using multi-type sensor. That framework was validated on a bridge benchmark structure in laboratory conditions.

From the literature review above, it is evident that most OSP problems for strain measurements have been addressed in simulated FEMs or laboratory structures, with only a few applied to real-world structures. Moreover, the impact of OSP on parameter estimation using real data has been rarely investigated. To the best of the author's knowledge, these issues have not been thoroughly explored in the literature using the EfI method.

1.5. Open Access

In order to promote the use of the material developed in this project and to facilitate the correction of the TFM, the main codes developed have been left open in the following GitHub repository:

`https://github.com/asanchezlc/MasterEstructurasTFM_aslc`

Chapter 2

Theoretical Background

2.1. Dynamical systems

2.1.1. Dynamic Equations and Modal Parameters

Let us consider a Multi-Degree Of Freedom (MDOF) system, as depicted in Figure 2.1. This system is governed by the following system of Ordinary Differential Equations (ODEs) in the time domain:

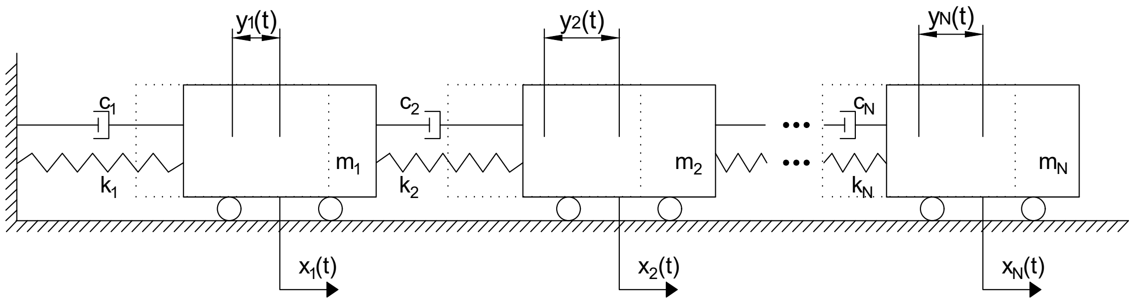

Figure 2.1: MDOF system.

$$\mathbf{M}\ddot{\mathbf{y}}(t) + \mathbf{C}\dot{\mathbf{y}}(t) + \mathbf{K}\mathbf{y}(t) = \mathbf{x}(t) \tag{2.1}$$

where:

- $\mathbf{M}$, $\mathbf{C}$, and $\mathbf{K}$ represent the mass, damping, and stiffness matrices, respectively, each of dimension $N \times N$; N is the number of Degrees of Freedom (DOFs).
- $\mathbf{x}(t)$ is the system input, a vector of forces of length N applied at each DOF.
- $\mathbf{y}(t)$ is the system output, a vector of displacements of length N corresponding to each DOF.

In the most general case, where the system is not classically damped (i.e. the damping matrix is not obtained as a linear combination of the mass and stiffness matrices), the solution of (2.1) can be obtained by transforming it into a state-space model. The state equation, directly derived from (2.1), reads:

$$\dot{\mathbf{s}}(t) = \mathbf{A}_c \mathbf{s}(t) + \mathbf{B}_c \mathbf{x}(t) \tag{2.2}$$

where:

- $\mathbf{s}(t) = \begin{pmatrix} \dot{\mathbf{y}}(t) \\ \mathbf{y}(t) \end{pmatrix}$ is the state vector.
- $\mathbf{A}_c = \begin{pmatrix} -\mathbf{M}^{-1}\mathbf{C} & -\mathbf{M}^{-1}\mathbf{K} \\ \mathbf{I} & \mathbf{0} \end{pmatrix}$ is the state matrix, with $\mathbf{I}$ being the identity matrix of dimension $N \times N$.
- $\mathbf{B}_c = \begin{pmatrix} \mathbf{M}^{-1} \\ \mathbf{0} \end{pmatrix}$ is the influence matrix.

The solution to equation (2.2) can be found by applying the Laplace transform to the state-space equation and obtaining the mode shapes $\boldsymbol{\phi}_n$ from the resulting eigenvalue problem (see [52, Chapter 5] for more details).

From the solution of the state-space equation, the solution of the system output in (2.1) in the frequency domain is:

$$\mathbf{y}(\omega) = \mathbf{H}(\omega)\mathbf{x}(\omega) \tag{2.3}$$

where $\mathbf{H}(\omega)$ the Frequency Response Function (FRF), and its expression is given by:

$$\mathbf{H}(\omega) = \sum_{n=1}^{N} \left(\frac{\mathbf{A}_n}{i\omega - \lambda_n} + \frac{\mathbf{A}_n^*}{i\omega - \lambda_n^*} \right) \tag{2.4}$$

where:

- $\mathbf{A}_n$ are the residues matrix, given by the following equation:

$$\mathbf{A}_n = \frac{\boldsymbol{\phi}_n \boldsymbol{\phi}_n^{\mathrm{T}}}{a_n}, \quad \text{with} \quad a_n = 2\lambda_n \boldsymbol{\phi}_n^{\mathrm{T}} \mathbf{M} \boldsymbol{\phi}_n + \boldsymbol{\phi}_n^{\mathrm{T}} \mathbf{C} \boldsymbol{\phi}_n \tag{2.5}$$

- λ_n are the poles of the system, given by the following expression:

$$\lambda_n = -\xi_n \omega_n + i\omega_n \sqrt{1 - \xi_n^2} \tag{2.6}$$

The solution of the system output in (2.1) in the time domain is:

$$\mathbf{y}(t) = \sum_{n=1}^{N} \left(\boldsymbol{\phi}_n e^{\lambda_n t} \right) + \sum_{n=1}^{N} \left(\boldsymbol{\phi}_n^* e^{\lambda_n^* t} \right) \tag{2.7}$$

The modal properties of the system are the natural undamped frequencies of vibration ($\omega_n = 2\pi f_n$), the displacement mode shapes ($\boldsymbol{\phi}_n$), and the damping ratios (ξ_n). The natural frequencies and damping ratios are obtained from the system's poles as follows:

$$f_n = \frac{\sqrt{\lambda_n \lambda_n^*}}{2\pi} \tag{2.8}$$

$$\xi_n = -\frac{\Re(\lambda_n)}{2\pi f_n} \tag{2.9}$$

Any dynamic identification method is aimed at determining these modal properties.

2.1.2. Strain Mode Shapes

When monitoring with strain sensors, the system output is not the displacement $\mathbf{y}(t)$, but the strain along a certain direction, which is defined as the ratio of deformation on that direction. Let $\boldsymbol{\epsilon}(t)$ be a vector containing the strain (along a specific direction) on each DOF of the system. The strain vector can be obtained from the displacement vector using the displacement-to-strain $\mathbf{S}$ matrix:

$$\boldsymbol{\epsilon}(t) = \mathbf{S}\mathbf{y}(t) \tag{2.10}$$

Thus, from equation (2.7), the expression of the strain can be obtained as:

$$\boldsymbol{\epsilon}(t) = \sum_{n=1}^{N} \left(\mathbf{S}\boldsymbol{\phi}_n e^{\lambda_n t}\right) + \sum_{n=1}^{N} \left(\mathbf{S}\boldsymbol{\phi}_n^* e^{\lambda_n^* t}\right) \tag{2.11}$$

The strain mode shapes are defined as:

$$\boldsymbol{\psi}_n = \mathbf{S}\boldsymbol{\phi}_n \tag{2.12}$$

Consequently, the Strain Frequency Response Function (SFRF) $\mathbf{H}^{\epsilon}(\omega)$ is defined as:

$$\boldsymbol{\epsilon}(\omega) = \mathbf{H}^{\epsilon}(\omega)\mathbf{x}(\omega) \tag{2.13}$$

where:

$$\begin{aligned}
\mathbf{H}^{\epsilon}(\omega) &= \mathbf{S}\mathbf{H}(\omega) \\
&= \sum_{n=1}^{N} \left(\frac{\mathbf{A}_n^{\epsilon}}{i\omega - \lambda_n} + \frac{\mathbf{A}_n^{\epsilon\,*}}{i\omega - \lambda_n{}^*} \right) \\
&= \sum_{n=1}^{N} \left(\frac{\boldsymbol{\psi}_n \boldsymbol{\phi}_n^{\mathrm{T}}}{a_n(i\omega - \lambda_n)} + \frac{\boldsymbol{\psi}_n{}^* \boldsymbol{\phi}_n^{*T}}{a_n{}^*(i\omega - \lambda_n{}^*)} \right)
\end{aligned} \tag{2.14}$$

Although not used in this Master Thesis, it is interesting to note that the SFRF contains both strain and displacement mode shapes. Consequently, when Experimental Modal Analysis is performed with strain sensors, both vectors can be obtained.

Note: Throughout this document, mode shapes are generally referred to as $\boldsymbol{\phi}$ for simplicity. However, it is important to clarify that all formulations and discussions pertain specifically to *strain mode shapes*, which are the output of the OMAs performed in this work.

2.2. Operational Modal Analysis

Operational Modal Analysis (OMA) technique allow the identification of modal properties from monitored systems subjected to ambient vibration (i.e., unknown random excitation). OMA techniques are commonly classified into two main groups: frequency-domain methods and time-domain methods [53]. In this work, one method from each family has been used to perform the dynamic identification of the case studies: Enhanced Frequency Domain Decomposition (EFDD), which is a frequency domain technique, and Covariance-Driven Stochastic Subspace Identification (COV-SSI), which is developed in the time domain.

The equations underlying the EFDD and COV-SSI methods are usually derived using the displacement mode shapes. Its derivation for strain mode shapes is completely analogous, as it only needs to include the **S** matrix described in Subsection 2.1.2.

2.2.1. EFDD

EFDD is an OMA technique aimed at extracting the modal parameters of a linear system based on an analysis in the frequency domain [54]. The starting point is the Frequency Domain Decomposition (FDD) method, which is explained as follows:

If the system of ODEs given in (2.1) is assumed to have real modes, the equation (2.7) can be simplified to:

$$\mathbf{y}(t) = \sum_{n=1}^{N} (\boldsymbol{\phi}_n q_n(t)) \tag{2.15}$$

where $q_n(t)$ are the modal coordinates. Note that this simplification is only assumed for clarity in the formulation. Nevertheless, extending this formulation for accommodating complex-valued (non classicaly) damped modes is straightforward by expanding the modal matrix $\boldsymbol{\phi}$ described hereafter with their complex counterparts. The Correlation Function Matrix $\mathbf{R_y}(\tau)$ is defined as $\mathbf{R_y}(\tau) \;= \mathbb{E}[\mathbf{y}(t)\mathbf{y}(t+\tau)^{\mathrm{T}}]$, with $\mathbb{E}$ denoting the expectation operator. Given that the modal matrix $\mathbf{\Phi} = [\boldsymbol{\phi_1}\, \boldsymbol{\phi_2} \,\ldots\, \boldsymbol{\phi_N}]$ is constant, and considering the modal expansion of the output response (Equation (2.15)), we have $\mathbf{R_y}(\tau) = \mathbf{\Phi}\mathbf{R_q}(\tau)\mathbf{\Phi}^{\mathrm{T}}$. Applying the Fourier transform to both sides of the equation, the following relation is obtained:

$$\mathbf{G_y}(f) = \mathbf{\Phi}\mathbf{G_q}(f)\mathbf{\Phi}^{\mathrm{T}} \tag{2.16}$$

where $\mathbf{G_y}(f)$ is the Cross Power Spectral Density (CPSD) matrix, defined as the Fourier transform of the Correlation Function Matrix, and f denotes the frequency variable. If the system is excited by stochastically independent forces described by a white Gaussian noise (a commonly accepted assumption in OMA), the modal coordinates are approximately uncorrelated, making $\mathbf{G_q}(f)$ a diagonal matrix. Thus, the Singular Value Decomposition (SVD) of the CPSD of the measured system output reads:

$$\mathbf{G_y}(f) = \mathbf{U}(f)\mathbf{\Sigma}(f)\mathbf{V}(f)^{\mathrm{H}} \tag{2.17}$$

with $\mathbf{U} = \mathbf{V}$ since the CPSD matrix is Hermitian and positive definite, and H superindex denoting the Hermitian transform. By comparing Equations (2.16) and (2.17), the singular vectors $\mathbf{U}(f)$ can be interpreted as the system mode shapes, and the singular values as the autospectral densities of the modal coordinates.

The starting point of the FDD method is the identification of the peaks in the first singular value[1] (the first diagonal element of the $\mathbf{\Sigma}(f)$ matrix). To achieve this, the so-called Singular Value Plot (SVP) is obtained (an example of a SVP is depicted in Figure 2.2). The mode shape associated with a resonant frequency can be obtained as the singular vector corresponding to that frequency value. Alternatively, it can be obtained as the average of the singular vectors weighted by the singular values belonging to the SDOF Bell, described below.

[1]Second or even third singular values may be used if the system has closely-spaced mode shapes.

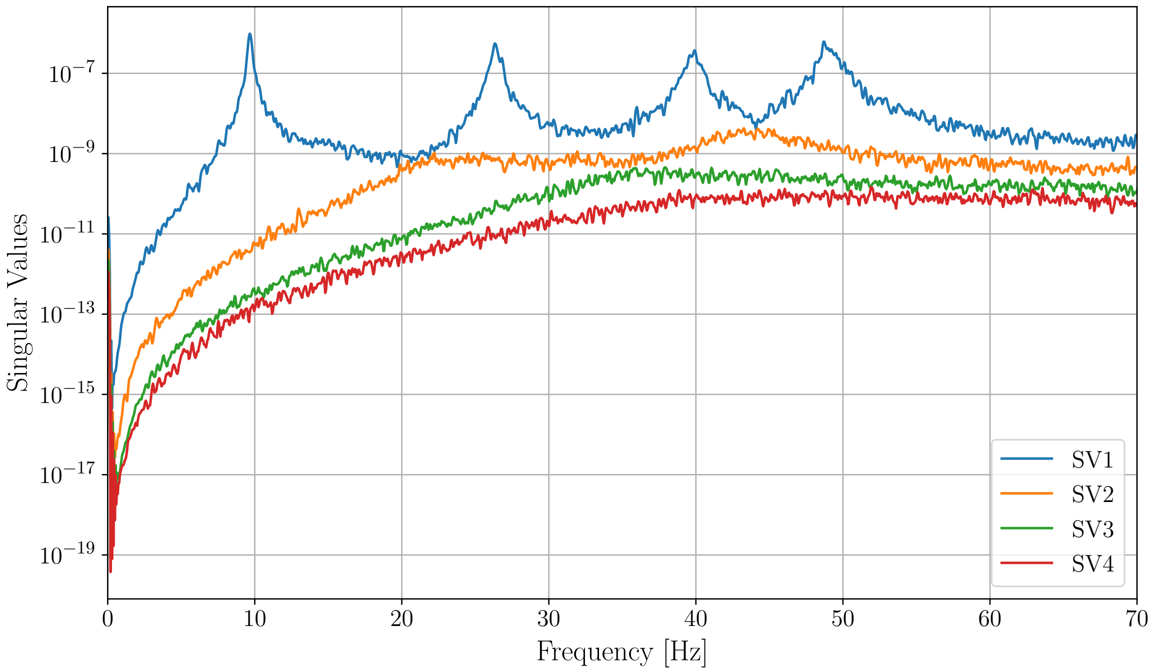

Figure 2.2: Sample SVP.

Once the peaks are identified, the damping properties can be extracted using the EFDD method. To this aim, the SDOF Bell (the set of singular values around a peak of the SVP, characterized by *similar* singular vectors) is extracted. The *similarity* between two mode shapes $\boldsymbol{\phi}_i$ and $\boldsymbol{\phi}_j$ is assessed by the Modal Assurance Criterion (MAC), defined as:

$$\mathrm{MAC}(\boldsymbol{\phi}_i, \boldsymbol{\phi}_j) = \frac{(\boldsymbol{\phi}_i^{\mathrm{T}} \boldsymbol{\phi}_j^*)^2}{(\boldsymbol{\phi}_i^{\mathrm{T}} \boldsymbol{\phi}_i^*)(\boldsymbol{\phi}_j^{\mathrm{T}} \boldsymbol{\phi}_j^*)} \in [0, 1] \tag{2.18}$$

The SDOF Bell is typically defined as the set of singular values around the resonant peak whose singular vectors comply with a certain MAC threshold RL, that is[2]:

$$s_1(f_j) \quad \text{such that} \quad \mathrm{MAC}(\mathbf{u}_1(f_i), \mathbf{u}_1(f_j)) > \mathrm{RL} \quad \forall j \tag{2.19}$$

where:

- f_i is the a frequency value at which a resonant peak $s_1(f_i)$ is found.
- s_1 is the first singular value (first diagonal element of the $\boldsymbol{\Sigma}(f)$ matrix).
- $\mathbf{u}_1$ is the first column of the singular vector matrix.
- RL is the Rejection Level (usually 0.8-0.9).

The SDOF Bell is used to obtain the modal properties of the system using a SDOF system identification method. For instance, a classical approach is the logarithmic decrement decay method using a representative portion of the Inverse Fourier Transform (IFT) of the SDOF Bell. Furthermore, the estimation of the damped frequency can be refined

[2]This definition can be easily adapted to use second or even third singular values.

by analysing the number of zero-crossing points of a representative portion of the IFT of the SDOF Bell.

When using the EFDD, it must be taken into account that the obtained modal properties are not exact; indeed, the assumption of the system output following (2.7) is an approximation, resulting in an FRF that does not exactly match the expression in equation (2.4). Nevertheless, this approximation is sufficiently accurate in cases where the modes are sufficiently spaced in frequency.

Algorithm 1 shows a pseudo-code of the EFDD technique. Note that in this simplified pseudo-code, modal properties are obtained using peaks from the first singular value, but the method can be easily generalized for using peaks from the second and even the third singular values.

Algorithm 1: EFDD Algorithm

Obtain $\mathbf{G_y}(f)$ from the measured system output $\mathbf{y}(t)$;
Perform SVD: $\mathbf{G_y}(f) = \mathbf{U}(f)\mathbf{\Sigma}(f)\mathbf{U}(f)^{\mathrm{H}}$;
Identify P peaks in $s_1(f)$;
for $i = 1$ **to** P **do**
  Calculate SDOF Bell =
   $\{s_1(f_j) \mid \mathrm{MAC}(\mathbf{u}_1(f_i), \mathbf{u}_1(f_j)) > \mathrm{RL},\ j = 1, \ldots, \dim(\mathbf{u}_1(f))\}$;
  Compute the IFT of the SDOF Bell;
  Obtain $f_{i,D}$ from the number of zero-crossings of the IFT(SDOF Bell);
  Estimate ξ_i by applying the logarithmic decrement to the IFT(SDOF Bell);
  Estimate $\boldsymbol{\phi_i} = \sum_k \mathbf{u}_1(f_k) \cdot s_1(f_k) \quad \forall f_k$ such that $s_1(f_k) \in$ SDOF Bell;
  Estimate $f_i = \frac{f_{i,D}}{\sqrt{1-\xi_i^2}}$;
end
return f_i, $\boldsymbol{\phi_i}$, ξ_i *for* $i = 1, \ldots, P$

2.2.2. COV-SSI

The COV-SSI is an OMA technique designed to extract the modal parameters of a linear system through time-domain analysis. To achieve this, a discrete-time stochastic state-space model is derived, and its state and output influence matrices are obtained[3]. From these matrices, the modal properties are extracted. The details are provided below:

The state-space model equation given in (2.2) is complemented by the observation equation, which provides the output measurements recorded by sensors positioned in l locations:

$$\mathbf{y}_l(t) = \mathbf{C}_a\ddot{\mathbf{y}}(t) + \mathbf{C}_v\dot{\mathbf{y}}(t) + \mathbf{C}_d\mathbf{y}(t) \tag{2.20}$$

where $\mathbf{y}_l$ represents the measurements in l locations (which in the most general case include displacement, velocity, and acceleration measurements); $\mathbf{C}_a$, $\mathbf{C}_v$, and $\mathbf{C}_d$ are the output location matrices for acceleration, velocity, and displacement, respectively.

This equation can be transformed using (2.1) into [54]:

$$\mathbf{y}_l(t) = \mathbf{C}_c\mathbf{s}(t) + \mathbf{D}_c\mathbf{x}(t) \tag{2.21}$$

where:

[3] Defined in equations (2.22) and (2.23).

- $\mathbf{C}_c = \begin{bmatrix}\mathbf{C}_v - \mathbf{C}_a\mathbf{M}^{-1}\mathbf{C} & \mathbf{C}_d - \mathbf{C}_a\mathbf{M}^{-1}\mathbf{K}\end{bmatrix}$ is the output influence matrix.
- $\mathbf{D}_c = \mathbf{C}_a\mathbf{M}^{-1}$ is the direct transmission matrix.

The state equation and the observation equation from (2.2) and (2.21) are expressed in continuous-time. For a given sampling period Δt (acquisition sampling frequency $f_s = 1/\Delta t$), the continuous-time equations can be discretized and solved at all discrete time instants $t_k = k\Delta t$ from the following discrete-time state-space model [54]:

$$\mathbf{s}_{k+1} = \mathbf{A}\mathbf{s}_k + \mathbf{B}\mathbf{x}_k \tag{2.22}$$

$$\mathbf{y}_{k,l} = \mathbf{C}\mathbf{s}_k + \mathbf{D}\mathbf{x}_k \tag{2.23}$$

where $\mathbf{A} = e^{\mathbf{A}_c\Delta t}$, $\mathbf{B} = (\mathbf{A} - \mathbf{I})\mathbf{A}_c^{-1}\mathbf{B}_c$, $\mathbf{C} = \mathbf{C}_c$ and $\mathbf{D} = \mathbf{D}_c$ for an input piecewise constant over the sampling period (zero-order hold).

When the unknown input excitation is assumed to follow a white noise distribution, the discrete-time state-space model can be converted into the following discrete-time stochastic state-space model:

$$\mathbf{s}_{k+1} = \mathbf{A}\mathbf{s}_k + \mathbf{w}_k \tag{2.24}$$

$$\mathbf{y}_{k,l} = \mathbf{C}\mathbf{s}_k + \mathbf{v}_k \tag{2.25}$$

where $\mathbf{w_k}$ and $\mathbf{v_k}$ combine the unknown excitation and process and measurement noise, all assumed to be white noise.

The COV-SSI method allows the identification of the matrices $\mathbf{A}$ and $\mathbf{C}$, from which the modal properties are obtained, by simple eigenvalue decomposition as shown henceforth.

The starting point for the obtention of $\mathbf{A}$ and $\mathbf{C}$ matrices is the computation of the covariance matrices $\mathbf{R}_i$, defined as:

$$\mathbf{R}_i = \frac{1}{N_S - i}\mathbb{E}\left[\mathbf{Y}(t)_{1:N_S-i}\mathbf{Y}(t)_{i:N_S}^{\mathrm{T}}\right] \tag{2.26}$$

where N_S is the total number of samples, $\mathbf{Y}(t)_{1:N_S-i}$ is a matrix containing all measurements in l outputs except the last i samples, $\mathbf{Y}(t)_{i:N_S}$ is a matrix containing all measurements in l outputs except the first i samples, and $i = 1, \ldots, 2j_b - 1$ where j_b is the main parameter of the algorithm, referred to as the time lag parameter.

The covariance matrices are then arranged in Toeplitz matrix:

$$\mathbf{T} = \begin{bmatrix} \mathbf{R}_{j_b} & \cdots & \mathbf{R}_1 \\ \vdots & \ddots & \vdots \\ \mathbf{R}_{2j_b-1} & \cdots & \mathbf{R}_{j_b} \end{bmatrix} \tag{2.27}$$

Given the stationarity properties of the state vector and the noise, the following recursive relations are satisfied [55]:

$$\mathbf{R_i} = \mathbf{C}\mathbf{A}^{i-1}\mathbf{G} \tag{2.28}$$

$$\mathbf{R_{-i}} = \mathbf{G}^{\mathrm{T}}(\mathbf{A}^{i-1})^{\mathrm{T}}\mathbf{C}^{\mathrm{T}} \tag{2.29}$$

where $\mathbf{G} = \mathbb{E}[\mathbf{s}_{k+1}\mathbf{y}_k^{\mathrm{T}}]$. Consequently, the Toeplitz matrix can be decomposed as $\mathbf{T} = \mathbf{O}\boldsymbol{\Gamma}$, where $\mathbf{O}$ is the observability matrix and $\boldsymbol{\Gamma}$ is the controllability matrix:

$$\mathbf{O} = \begin{bmatrix} \mathbf{C} \\ \mathbf{CA} \\ \vdots \\ \mathbf{CA}^{i-1} \end{bmatrix} \quad \text{and} \quad \boldsymbol{\Gamma} = \begin{bmatrix} \mathbf{A}^{i-1}\mathbf{G} & \cdots & \mathbf{AG} & \mathbf{G} \end{bmatrix} \tag{2.30}$$

The SVD of the Toeplitz matrix reads:

$$\mathbf{T} = \mathbf{U}\boldsymbol{\Sigma}\mathbf{V}^{\mathrm{T}} = \begin{bmatrix} \mathbf{U}_1 & \mathbf{U}_2 \end{bmatrix} \begin{bmatrix} \boldsymbol{\Sigma}_1 & 0 \\ 0 & 0 \end{bmatrix} \begin{bmatrix} \mathbf{V}_1 \\ \mathbf{V}_2 \end{bmatrix} \tag{2.31}$$

which allows us to obtain the observability and the controllability matrices as:

$$\mathbf{O} = \mathbf{U}_1\boldsymbol{\Sigma}_1^{1/2} \tag{2.32}$$

$$\boldsymbol{\Gamma} = \boldsymbol{\Sigma}_1^{1/2}\mathbf{V}_1^{\mathrm{T}} \tag{2.33}$$

Once the matrices $\mathbf{O}$ and $\boldsymbol{\Gamma}$ are computed, $\mathbf{C}$ is obtained as the first block element of the observability matrix (see Equation (2.30)), and $\mathbf{A}$ can be obtained through a least-squares problem, resulting in[4]:

$$\mathbf{A} = \boldsymbol{\Sigma}_1^{-1/2}\mathbf{U}_1^{\mathrm{T}}\mathbf{T}_2\mathbf{V}_1\boldsymbol{\Sigma}_1^{-1/2} \tag{2.34}$$

where

$$\mathbf{T}_2 = \begin{bmatrix} \mathbf{R}_{j_b+1} & \cdots & \mathbf{R}_2 \\ \vdots & \ddots & \vdots \\ \mathbf{R}_{2j_b} & \cdots & \mathbf{R}_{j_b+1} \end{bmatrix} \tag{2.35}$$

From this matrix, the modal parameters are obtained as follow [54]:

- The eigenvalue decomposition of $\mathbf{A}$ results in $\mathbf{A} = \boldsymbol{\Psi}\mathbf{M}\boldsymbol{\Psi}^{-1}$.
- Modeshapes are obtained as: $\boldsymbol{\phi}_k = \mathbf{C}\boldsymbol{\Psi}_k$, where $\boldsymbol{\Psi}_k$ is the kth column of $\boldsymbol{\Psi}$.
- Poles are obtained as: $\lambda_k = \frac{\ln(\mu_k)}{\Delta t}$, where μ_k is the k-th diagonal element of $\mathbf{M}$.

In practical applications, due to noise and modeling inaccuracies, it often happens that the gap between non-zero and zero singular values of (2.31) is not clear, thus resulting in serious problems for the determination of the correct model order [54]. As a consequence, a conservative approach is adopted based on the overspecification of the order of the model, which is set large enough to ensure the identification of all physical modes.

Overmodeling introduces spurious poles, which can be either physical noise modes (e.g. poles of the excitation system) or mathematical modes (introduced as a result of the overestimation of the model order). The separation of physical poles from spurious mathematical ones can be facilitated by constructing the so-called stabilization diagram (Figure 2.3). By tracking the evolution of the poles for increasing model orders, the physical modes can be identified from alignments of stable poles, in terms of the associated

[4]Other options are also available (e.g., exploiting the shift structure of the observability matrix).

frequencies and damping ratios (extracted using Equations (2.8) and (2.9)) and mode shapes. Instead, spurious poles tend to be more scattered and typically do not stabilize. The alignments of stable poles can start at lower or higher values of the model order, depending on the level of excitation of the modes [54].

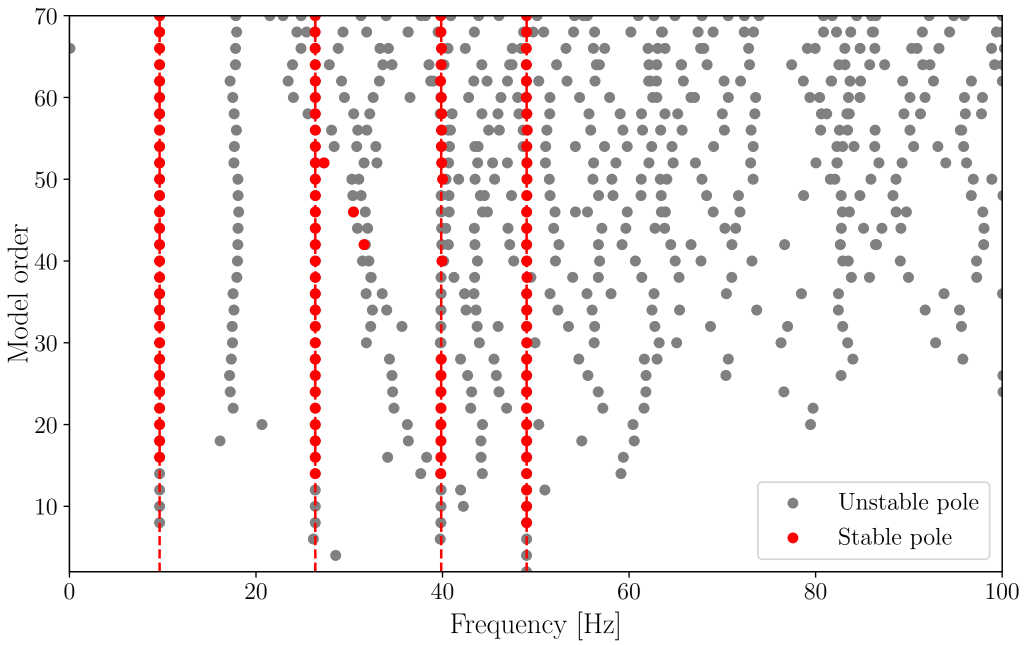

Figure 2.3: Sample stabilization diagram.

Algorithm 2 shows a pseudo-code of the COV-SSI technique.

2.3. OSP Problem

2.3.1. Problem Description

Let us consider a system with N DOFs and M mode shapes, from which only $n \leq N$ DOFs are accessible for monitoring using l available sensors (generally $l \ll n$).

An OSP problem consists in choosing the l optimal locations among the n accessible positions for placing the sensors in such a way that some variable (related to the information extracted from the sensors) is optimized.

In the context of OMA, the variable to be optimized is usually related to the quality of the measured modal parameters. If we consider a model with $m \leq M$ mode shapes of interest (referred to as target mode shapes), one approach is to maximize the linear independence of the extracted mode shapes. This is the approach of the EfI algorithm explained in below in Section 2.3.2.

2.3.2. Effective Independence (EfI) Method

EfI is an OSP algorithm first introduced by Kammer [38], in which the optimized variable is the linear independence of the measured mode shapes. The EfI algorithm involves a recursive process with $n - l$ iterations in which one DOF is removed at a time,

Algorithm 2: COV-SSI Algorithm

Input: Measured output ($\mathbf{Y}(t)$) $N_S \times l$, time lag j_b, maximum model order $o_{\max}$;
Initialize empty lists: `lamda_list`, `phi_list`;
for $i = 2$ **to** o_{max} 2 **do**
  Build $\mathbf{T}$ matrix (Eq. (2.27)) by computing $\mathbf{R}_i$ matrices (Eq. (2.26));
  Perform SVD on $\mathbf{T}$ (Eq. (2.31));
  Extract $\mathbf{O}$ (Eq. (2.32)) and $\mathbf{G}$ (Eq. (2.33)) matrices;
  Retrieve $\mathbf{C}$ matrix from first l columns of $\mathbf{O}$;
  Compute $\mathbf{A}$ from Eq. (2.34);
  Perform EVD of $\mathbf{A}$: $\mathbf{A} = \mathbf{\Psi}\mathbf{M}\mathbf{\Psi}^{-1}$;
  Initialize empty lists: `f_list_i`, `phi_list_i`, `xi_list_i`;
  for $k = 1$ **to** P **do**
    Compute $\lambda_k = \frac{\ln(\mu_k)}{\Delta t}$, where $\mu_k = \mathbf{M}_{k,k}$;
    Estimate $\boldsymbol{\phi}_k = \mathbf{C}\mathbf{\Psi}_k$;
    Append λ_k to `lambda_list_i`; $\boldsymbol{\phi}_k$ to `phi_list_i`;
  end
  Append `lambda_list_i` to `lambda_list`; `phi_list_i` to `phi_list`;
end
Obtain stable poles from `lambda_list_i` and `phi_list_i`;
Obtain frequencies and damping ratios from stable poles using Eq. (2.8) and Eq. (2.9);
Obtain modal properties by clustering stable frequencies, mode shapes, and damping ratios;
return *Modal properties*

corresponding to the DOF with the lowest contribution to the linear independence of the current mode shapes (i.e. sampled using the available DOFs in every iteration).

Let $\mathbf{\Phi}$ (dimension $k \times m$) be the mode shape matrix for k selected DOFs ($k = n$ for the first iteration, and $k = l \geq m$ at the end of the process). The m columns of $\mathbf{\Phi}$ are assumed to be linearly independent, so the FIM $\boldsymbol{Q} = \mathbf{\Phi}^{\mathrm{T}}\mathbf{\Phi}$ is symmetric and positive definite, and its EVD results in $\boldsymbol{Q} = \mathbf{\Psi}\mathbf{\Lambda}\mathbf{\Psi}^{\mathrm{T}}$, with $\mathbf{\Psi}$ being orthonormal and $\mathbf{\Lambda}$ containing real and positive eigenvalues. The columns of $\mathbf{\Psi}$ define a subspace of dimension m (called absolute identification space).

Taking into consideration that the i-th row of $\mathbf{\Phi}$ can be interpreted as the coordinates of the i-th DOF in the m target mode shapes, the rows of the matrix $\mathbf{\Phi\Psi}$ can be interpreted as the orthogonal projection of $\mathbf{\Phi}$ rows on the absolute identification space. Consequently, the matrix $\mathbf{J} = \mathbf{\Phi\Psi} \circ \mathbf{\Phi\Psi}$ ($\circ$ denotes element-wise product) is a matrix whose rows give the square of the proyection of $\mathbf{\Phi}$ rows in the absolute identification space.

$\mathbf{J}$ is a matrix such that its columns sum to the eigenvalues (calculated in the $\mathbf{\Lambda}$ matrix), so each element J_{ij} gives the contribution of row i of $\mathbf{\Phi}$ to the eigenvalue Λ_j. The normalization $\mathbf{F}_E = \mathbf{J}\mathbf{\Lambda}^{-1}$ results in a matrix with each element $F_{E,ij}$ containing the normalized contribution (between 0 and 1) of row i from $\mathbf{\Phi}$ to the eigenvalue j (with $\sum_i F_{E,ij} = 1$). Thus, defining $\mathbf{E}_D$ as a vector in which each element contains the sum of the rows of $\mathbf{F}_E$, each element $E_{D,i}$ of $\mathbf{E}_D$ represents the fractional contribution of the i-th DOF to the linear independence of $\mathbf{\Phi}$.

The EfI algorithm computes $\mathbf{E}_D$ at each iteration, and removes the DOF with the lowest associated value, resulting in a sub-optimal configuration (the iterative process does not ensure the optimal configuration is obtained) of sensors that measure highly independent mode shapes. The method is described in Algorithm 3.

Algorithm 3: EfI Algorithm

Initialize $\mathbf{\Phi}_k = \mathbf{\Phi}$ $(n \times m)$, DOFs = [1, 2, ..., n].
while $k > l$ **do**
  Compute FIM: $\boldsymbol{Q} = \mathbf{\Phi}_k^{\mathrm{T}} \mathbf{\Phi}_k$.
  Perform EVD of $\boldsymbol{Q}$: $\boldsymbol{Q} = \mathbf{\Psi \Lambda \Psi}^{\mathrm{T}}$.
  Compute $\mathbf{J} = (\mathbf{\Phi}_k \mathbf{\Psi}) \circ (\mathbf{\Phi}_k \mathbf{\Psi})$ (element-wise square) and $\mathbf{F}_E = \mathbf{J\Lambda}^{-1}$.
  Obtain $\mathbf{E}_D = [E_{D,1}, \ldots, E_{D,k}]$, where $E_{D,i} = \sum_{j=1}^{m} F_{E,ij}$.
  Get $i_{\min} = \arg\min(\mathbf{E}_D)$.
  Update $\mathbf{\Phi}_{k-1} = \mathbf{\Phi}_k$ with row $i_{\min}$ removed. Update DOFs removing element $i_{\min}$.
  $k = k - 1$.
end
return DOFs

The effectiveness of the EfI algorithm can be assessed with the AutoMAC matrix. For a set of m observed mode shapes, the AutoMAC matrix is obtained as:

$$\mathrm{AutoMAC}(\mathbf{\Phi}) = \begin{bmatrix} \mathrm{MAC}(\boldsymbol{\phi}_1, \boldsymbol{\phi}_1) & \cdots & \mathrm{MAC}(\boldsymbol{\phi}_1, \boldsymbol{\phi}_m) \\ \vdots & \ddots & \vdots \\ \mathrm{MAC}(\boldsymbol{\phi}_m, \boldsymbol{\phi}_1) & \cdots & \mathrm{MAC}(\boldsymbol{\phi}_m, \boldsymbol{\phi}_m) \end{bmatrix} \tag{2.36}$$

where $\mathrm{MAC}(\boldsymbol{\phi}_i, \boldsymbol{\phi}_j)$ is the function defined in Equation (2.18). The diagonal elements of the AutoMAC are equal to 1, while the off-diagonal elements are nearer to zero when the corresponding vectors i, j are less similar. Metrics such as the highest off-diagonal value or the off-diagonal mean values, can be used as quantitative measurements of the independence of the mode shapes.

2.4. Bayesian Parametric Inference

2.4.1. Inverse Problem for Stochastic Models

Let us consider a physical system from which we measure a set of experimental data $\mathbf{D} \in \mathcal{X}$. In order to predict its response, a deterministic model g can be defined as follows:

$$g : \Theta \to \mathcal{X} \tag{2.37}$$

$$\boldsymbol{\theta} \in \Theta \mapsto g(\boldsymbol{\theta}) = \boldsymbol{x} \in \mathcal{X} \tag{2.38}$$

where:

- $\boldsymbol{\theta}$: are the model parameters.
- $\boldsymbol{x}$: is the model response.
- $\Theta, \mathcal{X}$: are the subspaces of the model parameters and measured responses.

To assess the goodness of a model, a metric J that measures the distance between the model output $\boldsymbol{x}$ and the system data $\mathbf{D}$ is required. Mathematically:

$$J : \mathcal{X} \times \mathcal{X} \to \mathbb{R}, \quad (\boldsymbol{x}, \boldsymbol{D}) \mapsto J(\boldsymbol{x}, \boldsymbol{D}) \in \mathbb{R} \tag{2.39}$$

such that:

$$J(\boldsymbol{x_1}, \boldsymbol{D}) < J(\boldsymbol{x_2}, \boldsymbol{D}) \iff \boldsymbol{x_1} \text{ is } \textit{closer} \text{ to } \boldsymbol{D} \text{ than } \boldsymbol{x_2} \tag{2.40}$$

Given a metric J, a model g, and physical system data $\boldsymbol{D}$, an inverse problem consists of finding the parameters $\overline{\boldsymbol{\theta}} \in \Theta$ for which the model best predicts the experimental data, i.e., solving the optimization problem:

$$\overline{\boldsymbol{\theta}} = \arg\min_{\boldsymbol{\theta}} J(g(\boldsymbol{\theta}), \boldsymbol{D}) \tag{2.41}$$

Although a valid approach, the deterministic model g defined in equations (2.37) and (2.38) may not fully capture the physical system's behavior. In fact, two key factors should be considered:

- The physical system data $\boldsymbol{D}$ may be subject to measurement errors.
- The model g is only an approximation of the physical system and, as such, is subject to uncertainty.

To account for these uncertainties, a stochastic model $f(\boldsymbol{\theta}, \boldsymbol{Y})$ can be defined based on the deterministic model as follows:

$$f(\boldsymbol{\theta}, \boldsymbol{Y}) = g(\boldsymbol{\theta}) + \boldsymbol{Y} \tag{2.42}$$

where $\boldsymbol{Y}$ is a stochastic variable. Several aspects should be considered when defining $\boldsymbol{Y}$:

- $\boldsymbol{Y}$ is an element of $\mathcal{X}$, so that $\boldsymbol{x} + \boldsymbol{Y} \in \mathcal{X}$.
- $\mathbb{E}[\mathbf{Y}] = 0$, ensuring that the response is centered around $\boldsymbol{x} = g(\boldsymbol{\theta})$. Note that, if required, a bias parameter can be directly introduced in g as an additional parameter in $\boldsymbol{\theta}$.
- The covariance matrix of $\boldsymbol{Y}$, $\boldsymbol{\Sigma}$, can be assumed to bound the stochastic response.
- The Probability Density Function (PDF) of $\boldsymbol{Y}$ should satisfy the Principle of Maximum Entropy (PME) to account for all uncertainties.

Considering these factors, if $\boldsymbol{x}$ is unbounded, the PDF of the stochastic model is given by:

$$f(\boldsymbol{\theta}, \boldsymbol{Y}) \sim \mathcal{N}(g(\boldsymbol{\theta}), \boldsymbol{\Sigma}) \tag{2.43}$$

The inverse problem for the stochastic model in equation (2.43) can be formulated as finding the PDF of the parameters $\boldsymbol{\theta} \in \Theta$ given the measurements of the system data $\boldsymbol{D}$. In this approach, the stochastic model not only provides information about the parameters that better match the measurements, but it also quantifies the uncertainty surrounding them, i.e., their PDF [5].

To obtain the PDF of a set of parameters given the measured data and the model, Bayes' Theorem can be applied:

$$p(\boldsymbol{\theta}|\mathbf{D}, f) = \frac{p(\mathbf{D}|\boldsymbol{\theta}, f) \cdot p(\boldsymbol{\theta}|f)}{p(\mathbf{D}|f)} \tag{2.44}$$

where:

- $p(\boldsymbol{\theta}|\mathbf{D}, f)$: is the PDF of the parameters given the data and the model, also referred to as the *posterior* PDF; it is the goal of the inverse problem.

- $p(\mathbf{D}|\boldsymbol{\theta}, f)$: is called the *likelihood* function, representing the probability of the data given the parameters of the model. It directly depends on the assumed PDF of the stochastic model, and it quantifies the mismatch between the experimental data and the model predictions.

- $p(\boldsymbol{\theta}|f)$: is the *prior* PDF for the parameters. If only the interval of the possible parameters is known, the most uninformative prior distribution according to the PME is the uniform distribution.

- $p(\mathbf{D}|f)$: is called the *evidence*, representing the probability of the data given the model.

In equation (2.44), if $p(\boldsymbol{\theta}|f)$ is a uniform distribution and only one model is considered, one can write:

$$p(\boldsymbol{\theta}|\mathbf{D}, f) \propto p(\mathbf{D}|\boldsymbol{\theta}, f) \tag{2.45}$$

The likelihood value is determined using the metric defined in (2.39), which requires the computation of the model response $\boldsymbol{x}$.

In many cases, calculating $\boldsymbol{x}$ can be computationally expensive, especially when the parameter space Θ is large. As a result, obtaining the PDF of the model parameters through an exhaustive evaluation of the likelihood becomes impractical. Therefore, more efficient methods for sampling from the posterior distribution are needed. The MCMC methods, described in Section 2.4.3, offers an effective solution for this purpose.

2.4.2. Likelihood Computation using Modal Data

The likelihood computation presented in this section follows a methodology similar to that in [56].

When using modal data, the measured physical model data $\boldsymbol{D}$ usually consists of m measured frequencies and mode shapes obtained from the OMA, i.e.:

$$\boldsymbol{D} = \{\hat{f}_1, \ldots, \hat{f}_m, \hat{\boldsymbol{\phi}}_{\boldsymbol{1}}, \ldots, \hat{\boldsymbol{\phi}}_{\boldsymbol{m}}\} \tag{2.46}$$

[5] Metrics such as the Fisher Information provide insights into how much information is conveyed by the stochastic model. Although more information is generally desirable, the stochastic model is introduced specifically to account for uncertainties. Thus, the best model is not necessarily the one that maximizes information but the one that best accounts for uncertainties. This justifies using probability distributions that maximize information entropy according to the PME.

For a set of proposed parameters $\boldsymbol{\theta}$, the model obtains the modal data[6]:

$$g(\boldsymbol{\theta}) = \boldsymbol{x} = \{f_1, \ldots, f_m, \boldsymbol{\phi_1}, \ldots, \boldsymbol{\phi_m}\} \tag{2.47}$$

Assuming the errors in frequencies and mode shapes follow Gaussian distributions, one may write:

$$\boldsymbol{Y} = \{y_{f_1}, \ldots, y_{f_m}, \boldsymbol{y_{\phi_1}}, \ldots, \boldsymbol{y_{\phi_m}}\}, \quad \boldsymbol{\Sigma}^* = \{\sigma_{f_1}, \ldots, \sigma_{f_m}, \boldsymbol{\Sigma_{\phi_1}}, \ldots, \boldsymbol{\Sigma_{\phi_m}}\}. \tag{2.48}$$

Consequently, each frequency f_i follows a normal distribution $\mathcal{N}(\hat{f}_i, \sigma^2_{\hat{f}_i})$. Assuming that the standard deviation σ_{f_i} is proportional to the measured frequency $\hat{f}_i$, i.e., $\sigma_{f_i} = \sigma \cdot \hat{f}_i$, the likelihood of f_i given the data $\hat{f}_i$ is:

$$p(f_i) = \frac{1}{\sqrt{2\pi} \cdot \sigma \cdot \hat{f}_i} \exp\left(-\frac{(f_i - \hat{f}_i)^2}{2 \cdot \sigma^2 \cdot \hat{f}_i^{\,2}}\right) \tag{2.49}$$

Assuming stochastic independence[7] between the likelihoods of the frequencies, as well as proportional variance for all of them ($\sigma^2_{\hat{f}_i} = \sigma^2 \cdot \hat{f}_i^{\,2} \quad \forall i$) the likelihood of observing $f_1, \ldots, f_m$ given $\hat{f}_1, \ldots, \hat{f}_m$ is:

$$p(f_1, \ldots, f_m) = \prod_{i=1}^{m} p(f_i) = \frac{1}{(2\pi)^{m/2} \cdot \sigma^m \cdot \prod_{i=1}^{m} \hat{f}_i} \exp\left(-\frac{1}{2\sigma^2} \sum_{i=1}^{m} \frac{(f_i - \hat{f}_i)^2}{\hat{f}_i^{\,2}}\right) \tag{2.50}$$

With respect to the mode shapes, for simplicity, each mode $\boldsymbol{\phi_i}$ is assumed to follow a multivariate normal distribution $\mathcal{N}(\boldsymbol{\hat{\phi}_i}, \boldsymbol{\Sigma}^2_{\phi_i})$. Assuming that modal displacements are uncorrelated, the covariance matrix $\boldsymbol{\Sigma}_{\phi_i}$ is given by $\boldsymbol{\Sigma}_{\phi_i} = \frac{\sigma^2}{w} \cdot \mathrm{diag}(\|\boldsymbol{\hat{\phi}_i}\|^2)$, the likelihood of $\boldsymbol{\phi_i}$ given the data $\boldsymbol{\hat{\phi}_i}$ is:

$$p(\boldsymbol{\phi_i}) = \frac{1}{\left(2\pi \frac{\sigma^2}{w} \|\boldsymbol{\hat{\phi}_i}\|^2\right)^{n/2}} \exp\left(-\frac{w}{2\sigma^2} \frac{\|\boldsymbol{\phi_i} - \boldsymbol{\hat{\phi}_i}\|^2}{\|\boldsymbol{\hat{\phi}_i}\|^2}\right) \tag{2.51}$$

where:

- σ is a variable that introduces uncertainty related to frequencies.
- w_i is a variable that modulates the uncertainty introduced to the i-th modeshape. For simplicity, it is assumed that all modes exhibit identical variance, thus $w_i = w \quad \forall i$.

[6]The FEM model produces mode shapes $\boldsymbol{\phi'_i}$, typically mass normalized. In order to compare with the experimental mode shapes (arbitrary scaled), the numerical mode shapes are then scaled as: $\boldsymbol{\phi_i} = \beta_i \cdot \boldsymbol{\phi'_i}$, where $\beta_i = \frac{\boldsymbol{\hat{\phi}_i}^{\mathrm{T}} \boldsymbol{\phi_i}}{\|\boldsymbol{\phi_i}\|}$, minimizing $\|\boldsymbol{\hat{\phi}_i} - \beta_i \cdot \boldsymbol{\phi'_i}\|$.

[7]The stochastic independence shown in Equations (2.50) and (2.52) refers to information independence and should not be confused with causal independence. It is equivalent to asserting that if our information about ith frequency or mode is ‘good’ (e.g., large likelihood), this does not necessarily means that the information about the other modes must be equally good [57].

Again, assuming stochastic independence between the likelihoods of the mode shapes, the likelihood of observing $\boldsymbol{\phi_1}, \ldots, \boldsymbol{\phi_m}$ given $\hat{\boldsymbol{\phi}}_\mathbf{1}, \ldots, \hat{\boldsymbol{\phi}}_\boldsymbol{m}$ is:

$$p(\boldsymbol{\phi_1}, \ldots, \boldsymbol{\phi_m}) = \frac{1}{\left(2\pi \frac{\sigma^2}{w}\right)^{nm/2} \prod_{i=1}^{m} \|\hat{\boldsymbol{\phi}}_\boldsymbol{i}\|^n} \exp\left(-\sum_{i=1}^{m} \frac{w}{2\sigma^2} \frac{\|\boldsymbol{\phi_i} - \hat{\boldsymbol{\phi}}_\boldsymbol{i}\|^2}{\|\hat{\boldsymbol{\phi}}_\boldsymbol{i}\|^2}\right) \tag{2.52}$$

Assuming stochastic independence for both frequencies and mode shapes, the likelihood of the model output $\boldsymbol{x}$ (Equation (2.47)) given the data $\boldsymbol{D}$ (Equation (2.46)) is:

$$p(f_1, \ldots, f_m, \boldsymbol{\phi_1}, \ldots, \boldsymbol{\phi_m}) = \frac{1}{(2\pi)^{\frac{\overline{n}}{2}} \sigma^{\overline{n}} w^{nm/2} \prod_{i=1}^{m} \hat{f}_i \|\hat{\boldsymbol{\phi}}_\boldsymbol{i}\|^n} \exp\left(-\frac{1}{2\sigma^2} J\right) \tag{2.53}$$

where:

- $J = J_1 + wJ_2$, with $J_1 = \sum_{i=1}^{m} \frac{(f_i - \hat{f}_i)^2}{\hat{f_i}^2}$, and $J_2 = \sum_{i=1}^{m} \frac{\|\boldsymbol{\phi_i} - \hat{\boldsymbol{\phi}}_\boldsymbol{i}\|^2}{\|\hat{\boldsymbol{\phi}}_\boldsymbol{i}\|^2}$
- n is the dimension of the mode shapes $\boldsymbol{\phi_i}$.
- $\overline{n} = m + nm$

Note: For the remainder of this document, variables σ and w will be considered part of the model parameters. Consequently, the notation $f(\boldsymbol{\theta}, \boldsymbol{Y})$ will be simplied to $f(\boldsymbol{\theta})$.

2.4.3. Markov Chain Monte Carlo (MCMC) Methods

A Markov Chain is a sequence $X_0, X_1, \ldots$ of random elements of some set in which the conditional distribution of $X_{\zeta+1}$ given $X_0, \ldots, X_\zeta$ depends only on X_ζ. The set in which the X_ζ take values is called the *state space* of the Markov chain [58].

The joint distribution of a Markov chain is determined by:

- The marginal distribution of X_0, called the *initial distribution*[8].
- The conditional distribution of $X_{\zeta+1}$ given X_ζ, called the *transition probability distribution.*

If certain conditions related to the Markov Chain's ergodicity are satisfied (see [58, 59] for more details), then it has a stationary distribution. The idea behind MCMC algorithms is to construct a Markov Chain whose stationary distribution is the target PDF of the posterior PDF $p(\boldsymbol{\theta}|\mathbf{D}, f)$ of the model parameters [59].

One of the most widely used MCMC methods is the Metropolis Hastings [60, 61]. In this algorithm, a candidate model parameter $\boldsymbol{\theta}^*$ is sampled from a *proposal distribution* $q(\boldsymbol{\theta}^* \mid \boldsymbol{\theta}^{\zeta-1})$, given the state of the Markov Chain at step $\zeta - 1$. At the next state of the chain, ζ, the candidate parameter $\boldsymbol{\theta}^*$ is accepted (i.e., $\boldsymbol{\theta}^\zeta = \boldsymbol{\theta}^*$) with probability $1 - \min(1, r)$, where r is calculated as:

$$r = \frac{p(D \mid \boldsymbol{\theta}^*, f)\, p(\boldsymbol{\theta}^* \mid f)\, q(\boldsymbol{\theta}^{\zeta-1} \mid \boldsymbol{\theta}^*)}{p(D \mid \boldsymbol{\theta}^{\zeta-1}, f)\, p(\boldsymbol{\theta}^{\zeta-1} \mid f)\, q(\boldsymbol{\theta}^* \mid \boldsymbol{\theta}^{\zeta-1})} \tag{2.54}$$

[8]In the context of the Metropolis Hastings algorithm, it will be called the *prior* distribution.

This process is repeated until S samples are generated. An algorithmic description of the method is provided in Algorithm 4 (adapted from [59]).

Algorithm 4: M-H algorithm

Initialize $\boldsymbol{\theta}^{\zeta=0}$ by sampling from the prior PDF: $\boldsymbol{\theta}^0 \sim p(\boldsymbol{\theta}|f)$;
for $\zeta = 1$ **to** S **do**
    Sample from the proposal: $\boldsymbol{\theta}' \sim q(\boldsymbol{\theta}'|\boldsymbol{\theta}^{\zeta-1})$;
    Compute r from Eq. (2.54);
    Generate a uniform random number: $\alpha \sim \mathcal{U}[0,1]$;
    if $r \geqslant \alpha$ **then**
        Set $\boldsymbol{\theta}^{\zeta} = \boldsymbol{\theta}'$;
    else
        Set $\boldsymbol{\theta}^{\zeta} = \boldsymbol{\theta}^{\zeta-1}$;
    end
end
return $\boldsymbol{\theta}^{\zeta=0}, \ldots, \boldsymbol{\theta}^{\zeta=S}$

Chapter 3

Case Studies

3.1. Laboratory Steel Frame

3.1.1. Description of the Structure

The first case study involves the steel frame shown in Figure 3.1, located in the Laboratory of Sustainable Structural Engineering (SES-Lab). It is a steel structure with five floors, each 250 mm in height, and slabs measuring 250 mm by 500 mm. Each floor has four columns with rectangular sections of 30 mm by 2 mm and two beams, each 500 mm in length, composed of two T-profiles with a 30 mm base and height, and a thickness of 4 mm each.

The connections between the columns and the beams are semi-rigid, consisting of a small angle bracket fastened with four screws to the column and four screws to the beam (see Figure 3.2a).

Given the low ambient excitation levels registered in the laboratory, a 12V DC motor with an eccentric mass was placed on the upper floor of the structure, as depicted in Figure 3.2b. The motor is controlled with an Arduino Nano micro-controller, which allows to activate it at random time intervals with randomly varying rotational speeds.

The main goal of this case study is to validate the use of conventional SGs and low-cost electronic equipment to perform Operational Modal Analysis (OMA) in a controlled environment. Additionally, the effectiveness of the implemented Optimal Sensor Placement (OSP) technique will be assessed experimentally by comparing the quality[1] of the identified modal properties when using EfI locations compared to those based on engineering criteria. Achieving these objectives is a necessary step before monitoring a real structure.

3.1.2. Monitoring System

The monitoring system of the laboratory steel frame is formed by Strain Gauges (SGs). SGs (see Figures 1.1a and 3.4b) are sensors whose measured electrical resistance varies with changes in strain, thus allowing to monitor strain variations in structures. Nevertheless, direct measurement of the resistance variance is not achievable, as the changes are so small that they cannot be easily measured. To overcome this problem, a circuit formed by two series-parallel arrangements of equal resistances (one of them being

[1]In this case, the quality refers to the linear independence of the mode shpaes, assessed with the AutoMAC matrix as discussed in Section 2.3.2.

Figure 3.1: General view of the laboratory steel frame.

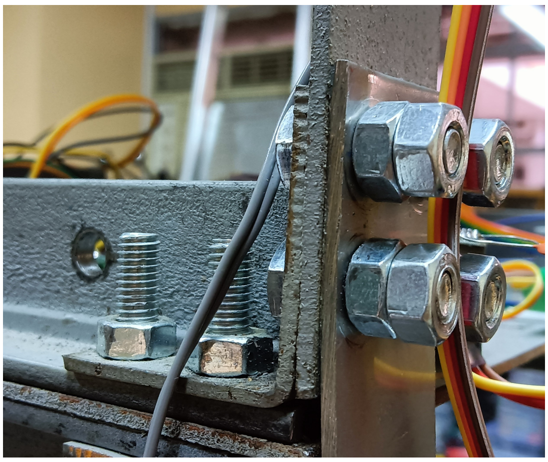

(a) Connections detail.

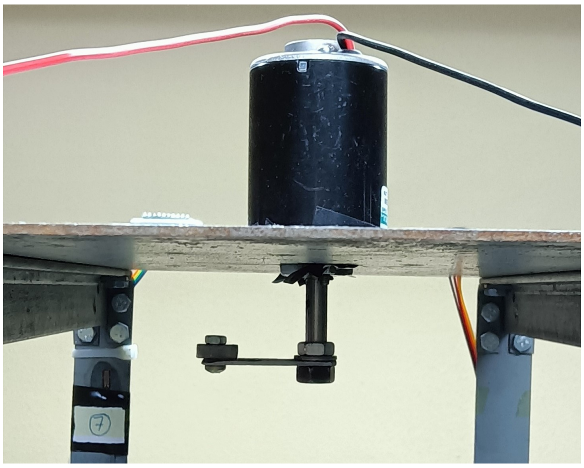

(b) 12V DC motor.

Figure 3.2: Images of the experimental setup.

the SG) connected between a voltage supply terminal and ground is built. This circuit is called Quarter Wheatstone bridge (see Figure 3.3), and is required for each of the SGs. The voltage difference between the two parallel branches is zero when the circuit is balanced, and changes when the SG resistance value differs from the other three, thus allowing to compute the strain in the sensor from that voltage [62].

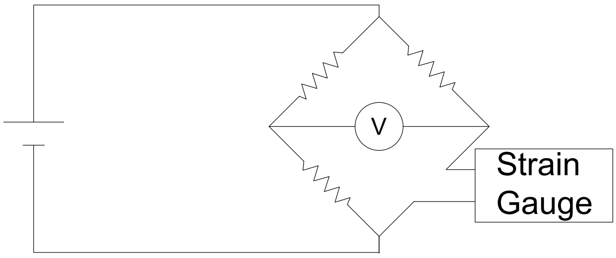

Figure 3.3: Quarter bridge schema.

(a) Arduino Mega.

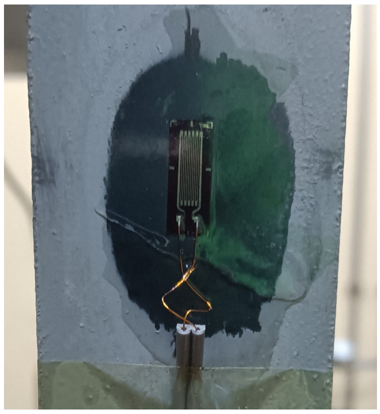

(b) Detail of a SG.

Figure 3.4: Photos of the electronic devices.

A Printed Circuit Board (PCB) has been designed[2] to facilitate the integration of the Wheatstone Bridge, as depicted in Figure 3.5a. The final PCB with its components is depicted in Figure 3.5b.

The electronic circuit is completed with the HX711 module, a signal amplifier and Analog to Digital Converter that allows to read the Wheatstone Bridge output and convert it into a digital value readable by the digital pins of the Arduino Mega microcontroller (Figure 3.4a).

The laboratory steel frame has been monitored with 17 SGs[3], recording dynamic measurements with a sampling rate of approximately 70 Hz. The areas where the SGs are located have been pre-treated by applying solvent to remove the paint. Then, the sensors have been bonded with conventional cyanoacrylate adhesive, and a protective polyurethane lacquer has been applied once placed. A detail of one of the installed SGs is depicted in Figure 3.4b.

The locations of the installed SGs are shown in Figure 3.6a, with their exact coordinates summarized in Table 3.1.

[2]Using *CircuitMaker* software.

[3]FLAB-6-11 from Tokyo Measuring Instruments Lab.

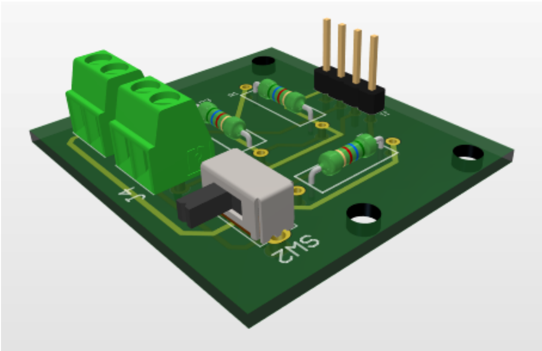

(a) Designed PCB.

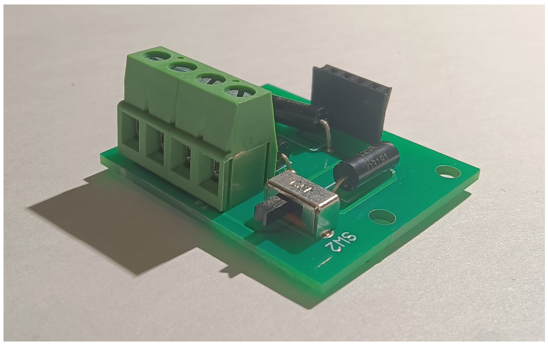

(b) Physical PCB.

Figure 3.5: Images of the PCB and its components for the integration of the Wheatstone Bridge.

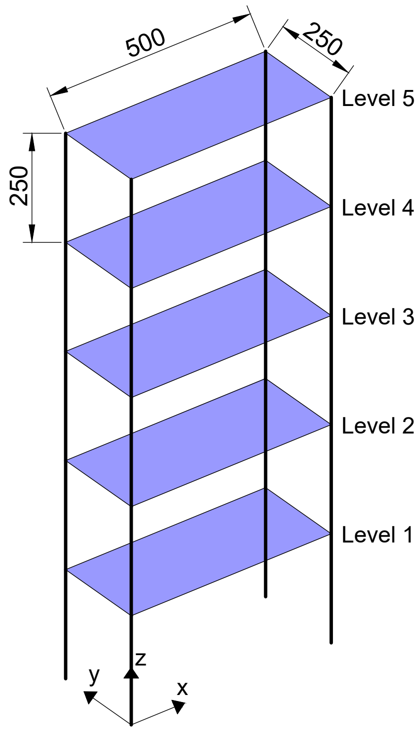

(a) Steel frame dimensions.

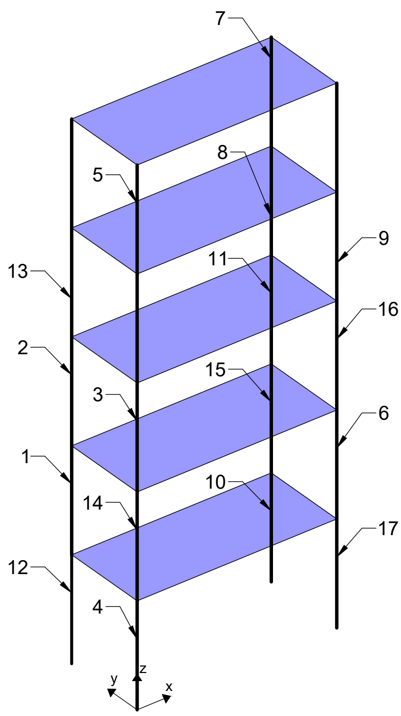

(b) SGs locations.

Figure 3.6: Laboratory steel frame.

Table 3.1: SGs location - steel frame

Channel	x (mm)	y (mm)	z (mm)
1	0	250	412.5
2	0	250	662.5
3	0	0	662.5
4	0	0	162.5
5	0	0	1162.5
6	500	0	412.5
7	500	250	1200
8	500	250	837.5
9	500	0	837.5
10	500	250	162.5
11	500	250	662.5
12	0	250	162.5
13	0	250	837.5
14	0	0	412.5
15	500	250	412.5
16	500	0	662.5
17	500	0	162.5

3.1.3. FEM and OSP Scheme

A Finite Element Model (FEM) of the laboratory steel frame has been developed using *SAP2000* software. The columns and beams were modeled as frame elements, while the slabs were modeled as shell elements. Special attention was given to the links: the base supports were modeled as fixed for displacements and as spring joints for bending in both directions. The connections between columns and beams were established using link linear elements, which were partially fixed for bending in both directions and for torsion. Additionally, the masses of the structure were carefully incorporated into the model.

The FEM updating is based on its modal parameters: natural frequencies and mode shapes. However, only a few of these parameters are used. On the one hand, the use of SGs restricts the measurements to only the x-direction, thus only bending modes in the x-direction and torsional modes are observable. On the other hand, the sampling frequency is around 70 Hz, limiting the highest observable modal parameters to 35 Hz (Nyquist frequency). Specifically, the modal parameters of interest are:

- Frequencies and strain mode shapes of the first five x-bending modes.
- Frequencies and strain mode shapes of the first torsional mode.

These six mode shapes, depicted in Figure 3.7, constitute the target modes of the OSP problem. For the candidate Degrees of Freedom (DOFs), only the columns of the structure were chosen as element were locating sensors. Specifically, 12 intermediate points along the midline of one of the larger faces of each of the columns were selected as candidate DOFs (see Figure 3.8).

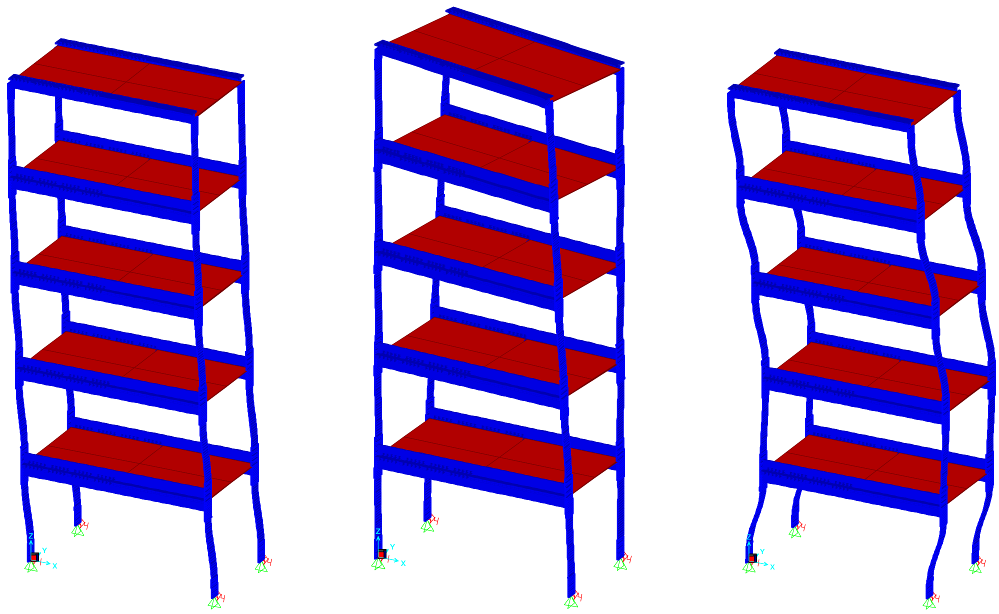

(a) Mode 1: 3.33 Hz. (b) Mode 2: 8.58 Hz. (c) Mode 3: 9.70 Hz.

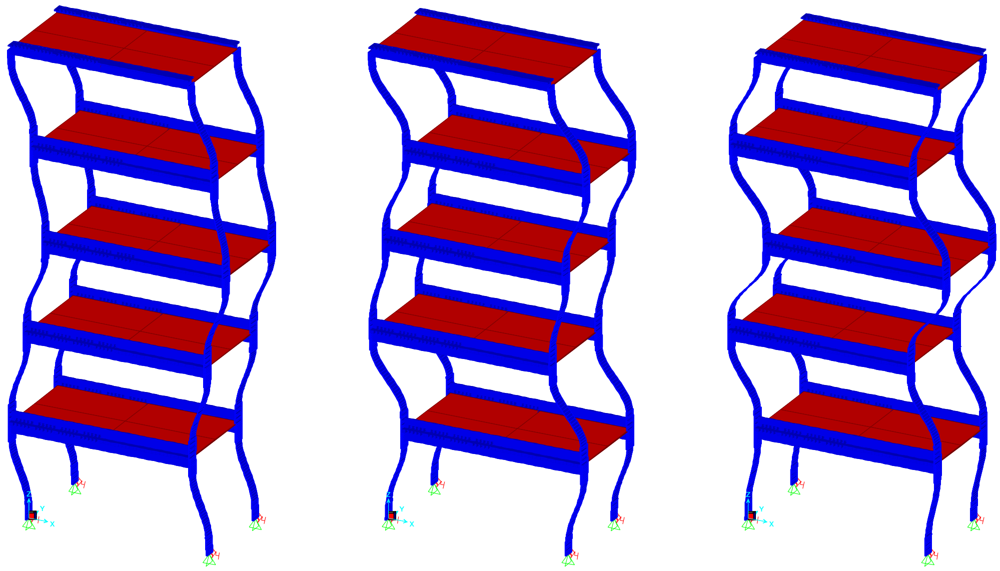

(d) Mode 4: 15.07 Hz. (e) Mode 5: 19.13 Hz. (f) Mode 6: 21.64 Hz.

Figure 3.7: Steel frame: target mode shapes for EfI algorithm and preliminar frequencies obtained by the FEM.

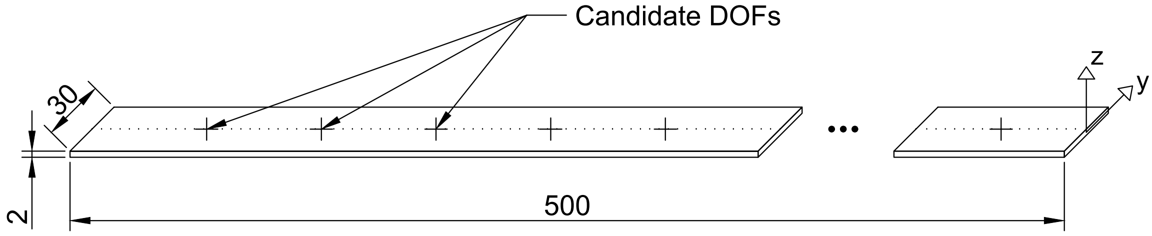

Figure 3.8: EfI algorithm - candidate DOFs in each column.

The strain mode shapes have been obtained from the element forces table in *SAP2000* for the modal load case. The transformation of these forces into strain modes has been carried out with the Navier's equation:

$$\varepsilon(y, z) = \frac{1}{E}\left(\frac{N}{A} - \frac{M_z}{I_z}y + \frac{M_y}{I_y}z\right) \tag{3.1}$$

where:

- A: Cross-sectional area.
- I_y, I_z: Moments of inertia about the y-axis and z-axis, respectively.
- N: Axial force.
- M_y, M_z: Bending moments about the y-axis and z-axis, respectively.
- E: Young's modulus.
- In this case, only $\varepsilon(0, t/2)$ is of interest, according to the notation used in Figure 3.8 (with t denoting the thickness of the column).

The EfI algorithm has been implemented in Python, obtaining the FEM characteristics from the *SAP2000 OAPI*. The number of SGs to be used satisfies $l \geq m$. A good compromise between the lower number of sensors and the higher linear independence of the modes (assessed by the lowest value of the E_D vector; see Figure 3.9) is found to be using eight SGs. The resulting optimal locations are depicted in Figure 3.10a.

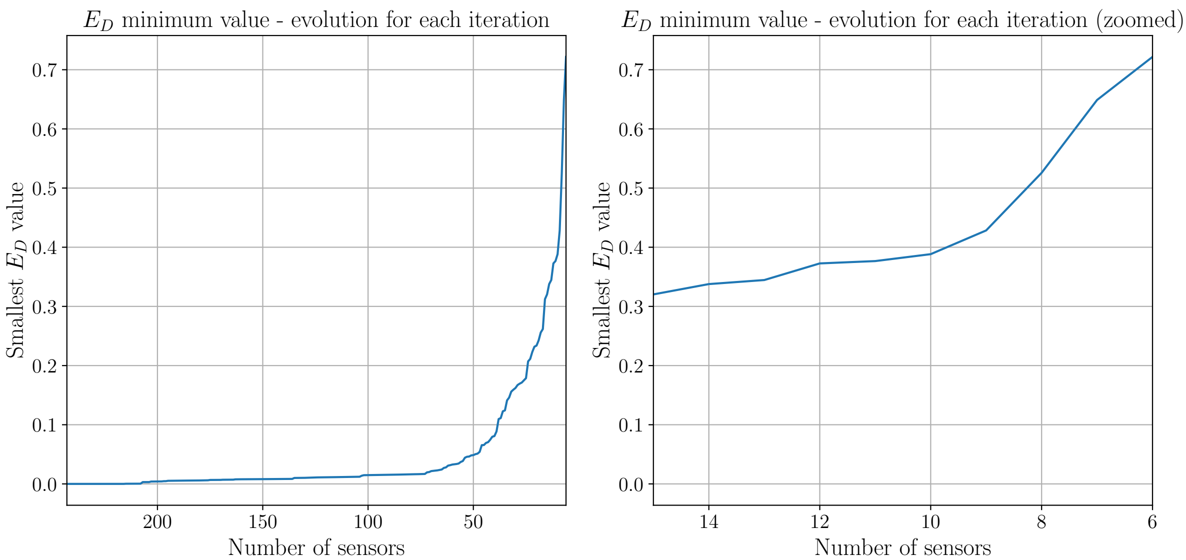

Figure 3.9: EfI Algorithm - E_D evolution for each iteration.

3.1.4. OMA Results

An OMA was conducted to assess the effectiveness of the EfI OSP configuration. The characteristics of the test are as follows:

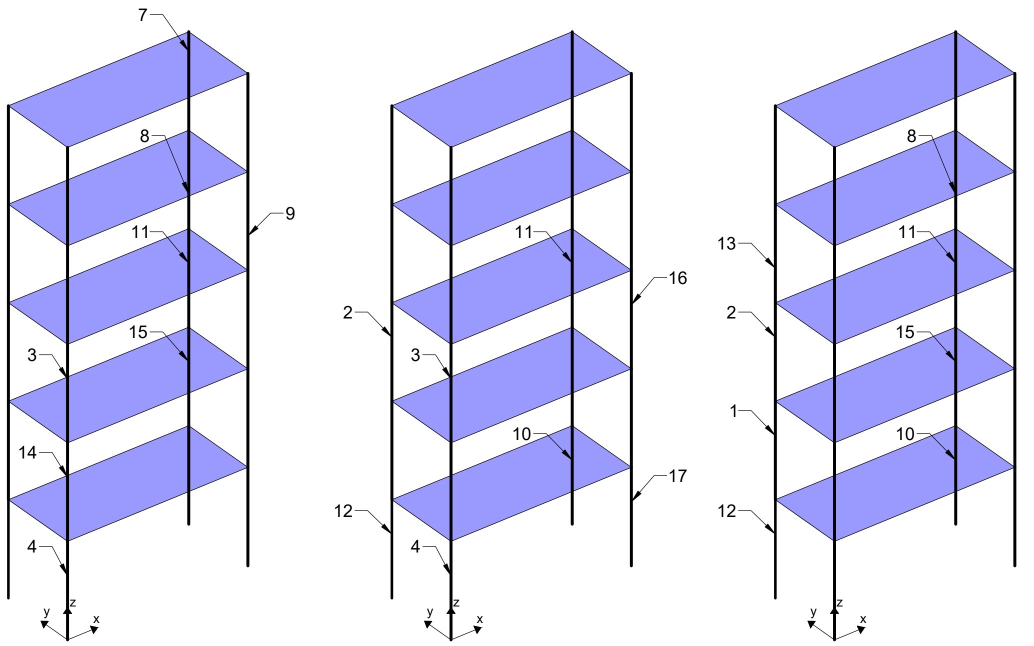

(a) SGs in Scheme A. (b) SGs in Scheme B. (c) SGs in Scheme C.

Figure 3.10: Steel frame: SGs configurations.

- Sampling frequency: $f_s = 72.83$ Hz.
- Test duration: 15 minutes, slightly exceeding the well-known rule of 2000 times the fundamental period T_1 (approximately 12 minutes and 20 seconds).
- Sensor layout: 17 SGs (locations shown in Figure 3.6b), corresponding to three different configurations: the EfI Optimal Scheme described in Section 3.1.3 (Figure 3.10a) and two additional sub-optimal configurations, simply defined following engineering intuition. Scheme B is a sub-optimal configuration that places one SG in each of the columns on the first and third floors (Figure 3.10b). Scheme C is a sub-optimal configuration that places one SG in each of the columns in the same x-z plane on the first four floors of the frame (Figure 3.10c). The channels for each scheme are listed in Table 3.2, and the coordinates of each channel are specified in Table 3.1.

Table 3.2: Selected channels for each configuration - steel frame

Scheme A (EfI-Optimal)	**Scheme B (Sub-optimal)**	**Scheme C (Sub-optimal)**
3	2	1
4	3	2
7	4	8
8	10	10
9	11	11
11	12	12
14	16	13
15	17	15

The raw signals of the 17 channels have been processed as follows:

- Application of a filter to remove outliers values (corresponding to electrical peak noise).
- Application of a Butterworth band-pass filter between 0.25 Hz and 35 Hz to remove signal trends and noise.

The data recorded from the first 6 channels by the Arduino microcontroller, after applying the initial filter, is shown in Figure 3.11. The signals have been centered to zero. It can be observed that the signals consist of pulses corresponding to the DC motor excitation.

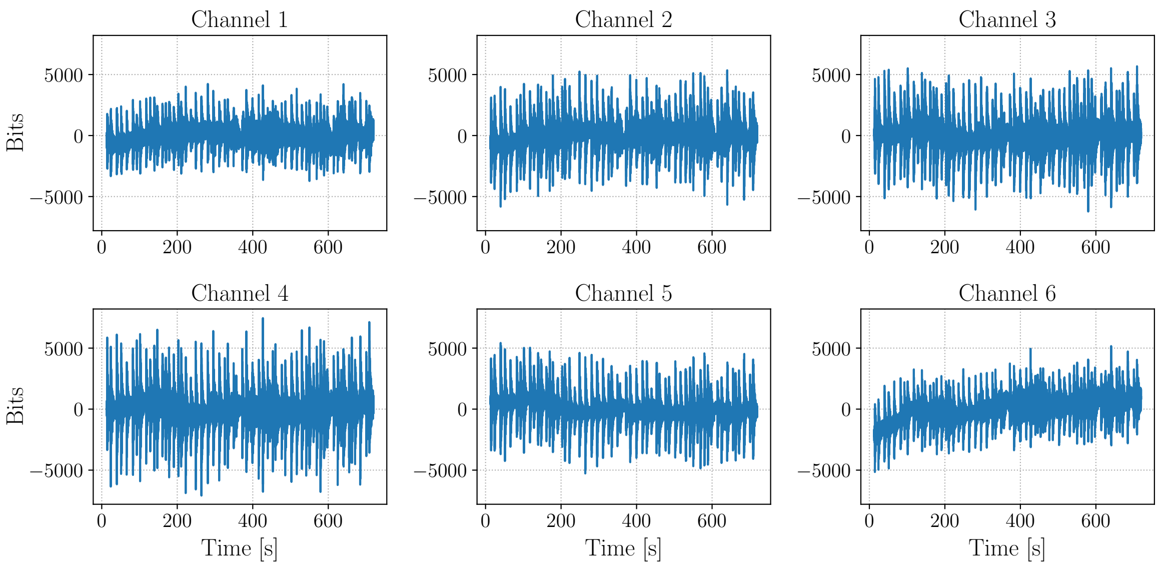

Figure 3.11: Measured data for channels 1 to 6 after removing electrical noise and centering the signals to have zero mean. The time series are shown in bits, as directly provided by the 24-bit analog-to-digital converter of the HX711 module. The conversion to physical strain is a simple linear transform using the gauge factor of the SGs, which does not affect the subsequent OMA.

All the target modes have been correctly identified through EFDD and COV-SSI algorithms for all three schemes. EFDD results have been used for the subsequent analysis.

The Singular Value Plot (SVP) of the Scheme A is illustrated in Figure 3.12. The frequencies of vibration (identified as peaks on it) are detailed in Table 3.3. It is worth to note that the torsional mode has been identified in the second singular value (as torsional and second x-bending mode are closely spaced). Additionally, the two peaks observed at 3.77 Hz and 20.87 Hz correspond to the two first modes in y-axis (whose mode shape cannot be identified due to the SGs direction of measurement). The strain mode shapes coordinates for the three schemes are set out in Appendix I.

The comparison of the strain mode shapes linear independence between the three SGs configurations (Scheme A - EfI Optimal - Scheme B and Scheme C) is made through the AutoMAC matrix, defined in equation (2.36). A graphical representation of the three AutoMAC matrices is depicted in Figure 3.13.

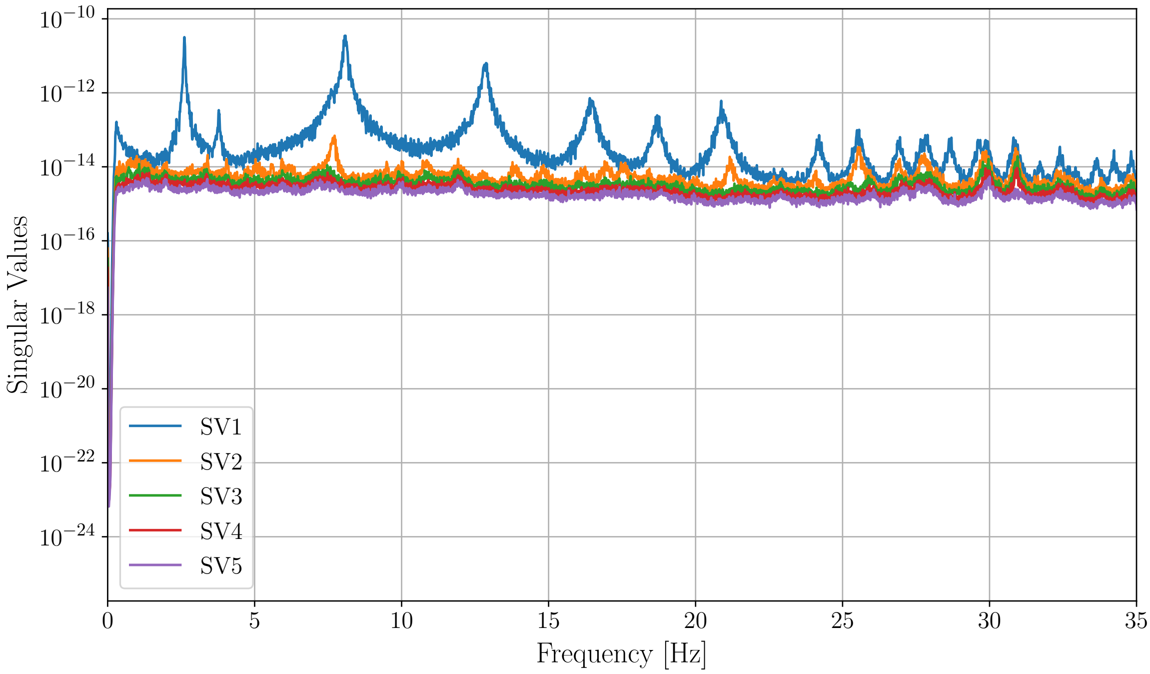

Figure 3.12: SVP for scheme A.

Table 3.3: Frequencies of vibration from OMA - steel frame

Mode Number	Frequency (Hz)	Type of Mode
1	2.611	x-bending
2	7.681	torsional
3	8.081	x-bending
4	12.843	x-bending
5	16.450	x-bending
6	18.692	x-bending

Table 3.4 collects the off-diagonal mean and highest values for the three AutoMAC matrices. It is observed from Figure 3.13a and from Table 3.4 that the Scheme A, corresponding to the EfI configuration, produces the best results, thus experimentally proving the effectiveness of this algorithm.

Table 3.4: Off-diagonal metrics for schemes A, B, and C - steel frame

	Off-diagonal mean value	**Off-diagonal highest value**
Scheme A	0.018	0.086
Scheme B	0.216	0.958
Scheme C	0.094	0.953

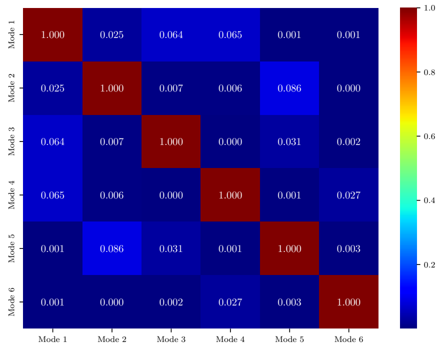

(a) AutoMAC Scheme A.

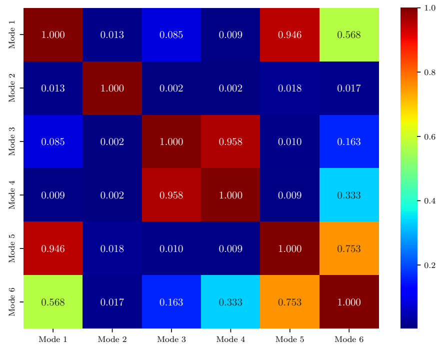

(b) AutoMAC Scheme B.

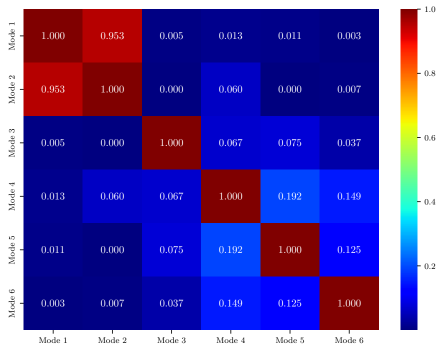

(c) AutoMAC Scheme C.

Figure 3.13: Comparison of the AutoMAC matrices for three configuration schemes.

3.1.5. Model Updating

Algorithm

The implemented algorithm follows a structure similar to Algorithm 4, with the following considerations:

1. The parameters of the structure subjected to uncertainty are:

   $a)$ Bending stiffness of the joint supports: k_{θ_y}, k_{θ_z}.

b) Bending stiffness of the connecting frames on all floors: $k_{1,My}$, $k_{1,Mz}$.

These parameters were selected after performing a sensitivity analysis of the variables affecting the modal properties. Consequently, the vector of parameters, expanded with the uncertainty variables σ, w (defined in Section 2.4.2), is:

$$\boldsymbol{\theta} = [\theta_1, \theta_2, \theta_3, \theta_4, \theta_5, \theta_6]^{\mathrm{T}} = [k_{\theta_y}, k_{\theta_z}, k_{1,My}, k_{1,Mz}, \sigma, w]^{\mathrm{T}} \tag{3.2}$$

2. The *prior distribution* of the model parameters is a uniform distribution:

$$\theta_{i|f} \sim \mathcal{U}(I_j) \tag{3.3}$$

where $I_j = [a_j, b_j]$ denotes the interval of the uniform distribution for the parameter θ_j. As a consequence, $p(\boldsymbol{\theta}) = \text{constant}\,\forall\,\boldsymbol{\theta}$. The following intervals have been considered[4]:

$$\begin{aligned} I_1 &= [0, 2\times 10^6]\,\mathrm{N/m} \\ I_2 &= [0, 5\times 10^5]\,\mathrm{N/m} \\ I_3 &= [0, 2\times 10^6]\,\mathrm{N/m} \\ I_4 &= [0, 10^6]\,\mathrm{N/m} \\ I_5 &= [0.005, 0.1] \\ I_6 &= [0.01, 1.5] \end{aligned} \tag{3.4}$$

3. The *proposal distribution* $q(\boldsymbol{\theta}^* \mid \boldsymbol{\theta}^{\zeta-1})$ is a multivariate normal distribution[5] given by:

$$q(\boldsymbol{\theta}^* \mid \boldsymbol{\theta}^{\zeta-1}) = \mathcal{N}(\boldsymbol{\mu_{\zeta-1}}, \boldsymbol{\Sigma}(\sigma_q)) \tag{3.5}$$

where:

- ζ is the number of the iteration.
- $\boldsymbol{\mu_{\zeta-1}} = \boldsymbol{\theta}^{\zeta-1}$
- $\boldsymbol{\Sigma}(\sigma_q) = \mathrm{diag}((\sigma_1)^2, \ldots, (\sigma_6)^2)$, with $\sigma_j = \sigma_q \times (b_j - a_j)$; σ_q is one of the main parameters of the algorithm. Increasing its value generally leads to a lower acceptance rate[6].

Consequently, $q(\boldsymbol{\theta}^{\zeta-1} \mid \boldsymbol{\theta}^*) = q(\boldsymbol{\theta}^* \mid \boldsymbol{\theta}^{\zeta-1})$

4. As a result of points 2 and 3, the factor r in Equation (2.54) simplifies to:

$$r = \frac{p(D \mid \boldsymbol{\theta}^*, f)}{p(D \mid \boldsymbol{\theta}^{\zeta-1}, f)} \tag{3.6}$$

[4]The upper limits of these intervals were established such that the absolute frequency difference between these values and the frequencies with infinite stiffness is less than 0.005 Hz for all modes.

[5]Strictly speaking, the *proposal distribution* is a truncated normal, as the proposed parameter θ_j^* is discarded if it falls outside the interval I_j. However, if the bounds of the interval are regions of very low likelihood (which is desirable), this effect is negligible.

[6]The optimal acceptance rate for the Metropolis-Hastings algorithm typically falls between 20% and 50% [63].

5. To avoid numerical issues arising from the computation of large exponential terms, the natural logarithm of the likelihoods is used[7]. The log-likelihood for the frequencies in Equation (2.50) is given by:

$$\log(p(f_1,\ldots,f_m)) = -\frac{m}{2}\log(2\pi) - m\log(\sigma) - \sum_{i=1}^{m}\log(\hat{f}_i) - \frac{1}{2\sigma^2}J_1 \tag{3.7}$$

The log-likelihood of the mode shapes (Equation (2.52)) is:

$$\log(p(\boldsymbol{\phi_1},\ldots,\boldsymbol{\phi_m})) = -\frac{nm}{2}\left(\log(2\pi)+\log\left(\frac{\sigma^2}{w}\right)\right) - n\sum_{i=1}^{m}\log(\|\hat{\boldsymbol{\phi}}_{\boldsymbol{i}}\|) - \frac{w}{2\sigma^2}J_2 \tag{3.8}$$

Finally, the full log-likelihood computation (Equation (2.53)) is:

$$\begin{aligned}\log(p(\boldsymbol{x})) = &-\frac{N}{2}\log(2\pi) - N\log(\sigma) - \sum_{i=1}^{m}\log(\hat{f}_i) \\ &+\frac{nm}{2}\log(w) - \sum_{i=1}^{m} n\log(\|\hat{\boldsymbol{\phi}}_{\boldsymbol{i}}\|) - \frac{1}{2\sigma^2}J\end{aligned} \tag{3.9}$$

where the terms $-\frac{N}{2}\log(2\pi) - \sum_{i=1}^{m}\log(\hat{f}_i) - \sum_{i=1}^{m} n\log(\|\hat{\boldsymbol{\phi}}_{\boldsymbol{i}}\|)$ can be omitted, as they are constant.

6. Due to the presence of closely-spaced mode shapes, a mode matching strategy is necessary to ensure accurate comparison between the measured modal properties and the FEM modal properties. The MAC has been used for mode matching with the following criterion: f_i^{FEM} corresponds to f_j^{Data} if and only if $MAC(\boldsymbol{\phi_i},\boldsymbol{\phi_j}) > MAC(\boldsymbol{\phi_i},\boldsymbol{\phi_k})$ for all $k \neq j$.[8]

The pseudo-code of the implemented algorithm is detailed in Algorithm 5.

Results

In a first approach, Algorithm 5 was implemented to perform the parametric Bayesian inference. After preliminary tests, a value of $\sigma_q = 0.00009$ was selected[9], resulting in an acceptance rate of approximately 17.5%. A total of 100,000 iterations were performed, during which the convergence was notably slow (convergence was assessed based on the expectation of the log-likelihood). Furthermore, the algorithm showed limited exploration of the parameter space within their intervals, likely due to the small value of σ_q adopted. These issues were attributed to the interaction between the two uncertain parameters, σ and w, as well as the reduced value of σ_q, which negatively affected the convergence.

[7] This does not affect the results, as the logarithmic function is monotonically increasing

[8] This criterion has been deemed sufficient due to the high linear independence of the modes ensured by the EfI algorithm.

[9] Typical values of σ_q range from 0.01 to 0.05; however, a very low acceptance rate was observed, requiring a significant reduction.

Algorithm 5: Implemented M-H Algorithm

Input: σ_q, $I_1 \dots I_6$, S ;
Initialize $\boldsymbol{\theta}^{\zeta=0}$ by sampling from uniform distributions;
for $\zeta = 1$ **to** S **do**
    Sample from the proposal distribution: $\boldsymbol{\theta}' \sim q(\boldsymbol{\theta}' \mid \boldsymbol{\theta}^{\zeta-1})$;
    Obtain the *SAP2000* modal response;
    Match modal properties based on the highest MAC value;
    Compute $\log(p(D \mid \boldsymbol{\theta}^*, f))$ and $\log(p(D \mid \boldsymbol{\theta}^{\zeta-1}, f))$ using Eq. (3.9);
    Calculate $\log(r)$ from Eq. (3.6); $\log(r) = \log(p(D \mid \boldsymbol{\theta}^*, f)) - \log(p(D \mid \boldsymbol{\theta}^{\zeta-1}, f))$;
    Generate a uniform random number: $\alpha \sim \mathcal{U}[0, 1]$;
    if $\exp(\log(r)) \geq \alpha$ **then**
        Set $\boldsymbol{\theta}^{\zeta} = \boldsymbol{\theta}'$;
    else
        Set $\boldsymbol{\theta}^{\zeta} = \boldsymbol{\theta}^{\zeta-1}$;
    end
end
return $\boldsymbol{\theta}^{\zeta=0}, \dots, \boldsymbol{\theta}^{\zeta=S}$

To further investigate the problem, a new inference was conducted using a simplified approach: only the frequencies were used to compute the likelihood (as per Equation (2.50), and Equation (3.7) for the log-likelihood), thereby eliminating the uncertainty parameter associated with the mode shapes, w. The convergence diagram for this inference is shown in Figure 3.14. Based on this diagram, the burn-in period (initial set of samples disregarded in the final chain) was determined to be 80,000 iterations, resulting in a mean acceptance rate of 4.92%.

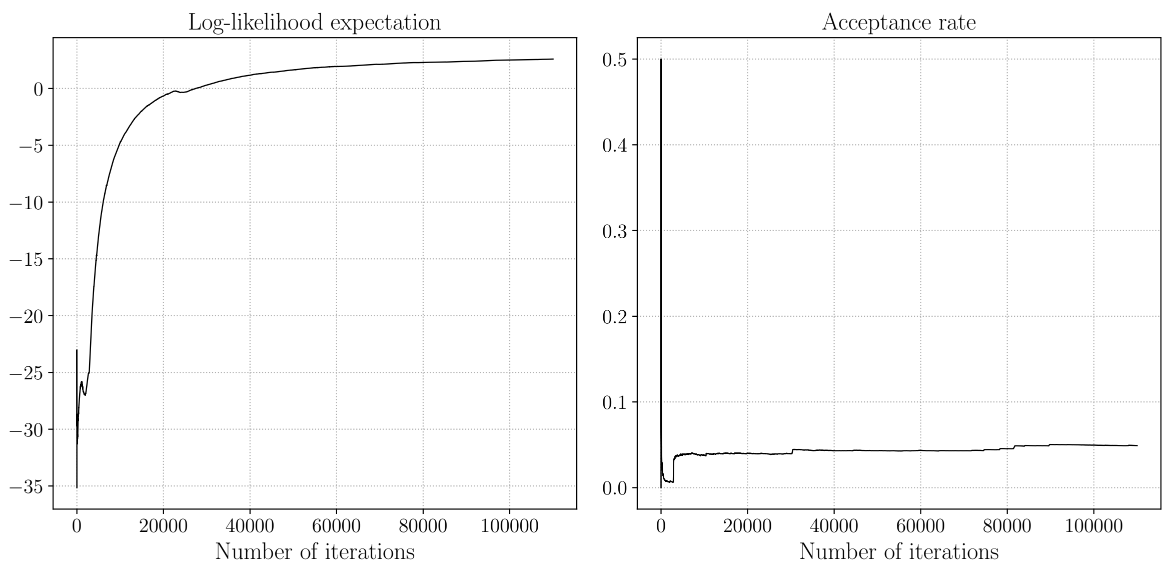

Figure 3.14: Convergence diagram.

The sample 103,100 registered the highest value of likelihood. The parameters associated to that sample are:

$$
\begin{aligned}
k_{\theta_y} &= 1.116 \times 10^{6}\,\mathrm{N/m} \\
k_{\theta_z} &= 4.617 \times 10^{5}\,\mathrm{N/m} \\
k_{1,My} &= 1.793 \times 10^{6}\,\mathrm{N/m} \\
k_{1,Mz} &= 6.903 \times 10^{2}\,\mathrm{N/m} \\
\sigma &= 8.766 \times 10^{\text{-}2}
\end{aligned}
\tag{3.10}
$$

Table 3.5 presents a comparison of the frequencies from the original FEM and the updated FEM (with parameters from Equation (3.10)) against the experimental data. It can be seen that the updated model is significantly more accurate.

Table 3.5: Comparison between experimental frequencies and FEM predictions for both uncalibrated and calibrated models.

Mode	Experimental	Uncalibrated		Calibrated	
	Freq. [Hz]	Freq. [Hz]	R. Error [%]	Freq. [Hz]	R. Error [%]
1	2.611	3.330	27.54	2.773	6.20
2	7.681	8.582	11.73	8.487	10.49
3	8.081	9.701	20.05	8.023	-0.71
4	12.843	15.072	17.36	12.363	-3.74
5	16.450	19.134	16.31	15.598	-5.18
6	18.692	21.641	15.78	17.449	-6.65

The posterior Probability Density Function (PDF) of the inferred parameters is shown in Figure 3.15, where one out of every fifty samples after the burn-in period was retrieved to mitigate correlation effects.

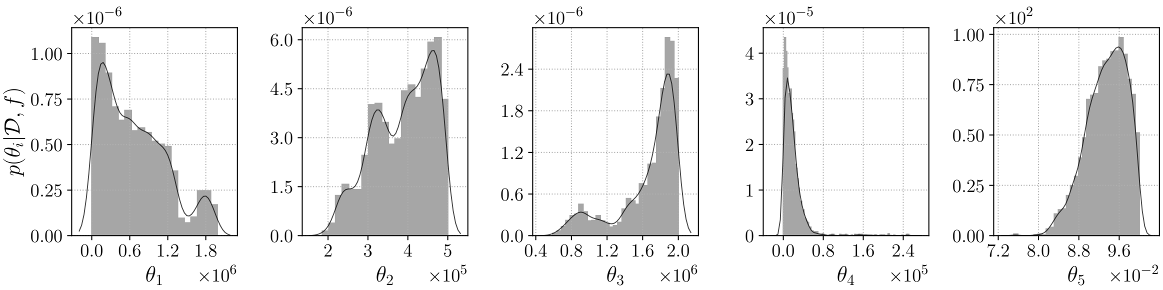

Figure 3.15: PDF of the inferred parameters.

To further analyse the results, the frequencies of the FEM model for each retrieved sample is presented in Figure 3.16. It can be observed that the model's performance is poor, generally overestimating the frequencies and introducing significant bias.

The poor model performance has been attributed to several factors. Firstly, although the inference considered only frequencies, the comparison was based on a pre-established mode matching process, which introduced important errors in some cases.

For example, the second output frequency from the FEM model for sample 7,717 was 2.417 Hz, corresponding to the first torsional mode. However, the algorithm identified the first torsional mode with the fifth output frequency, which had a value of 5.772 Hz. In

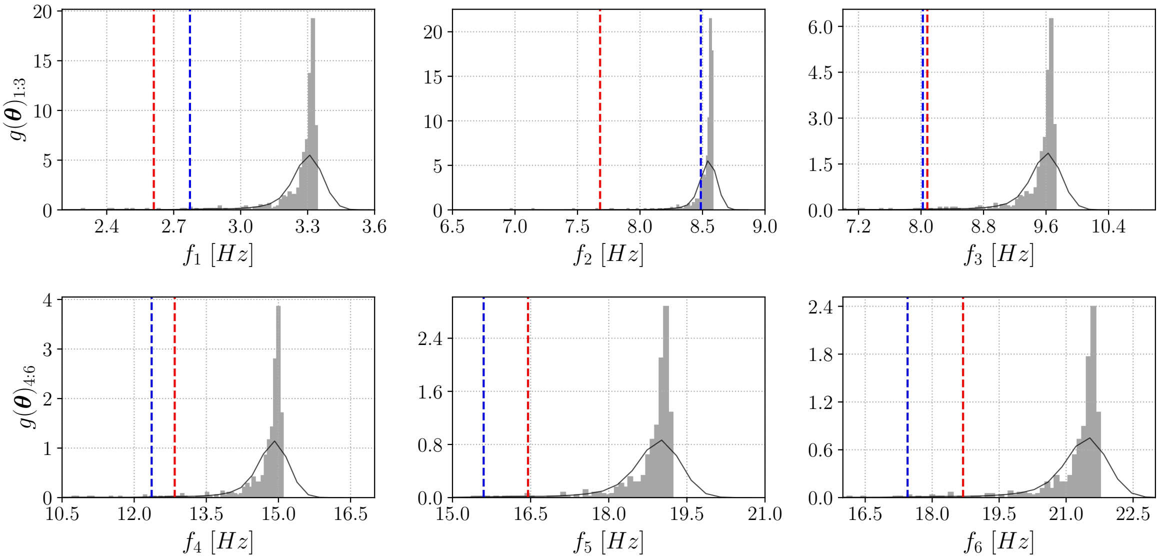

Figure 3.16: Model predictions. The PDF was obtained using Kernel Density Estimation; the frequency identified by OMA is represented by a dashed vertical red line; the frequency corresponding to the parameters with highest likelihood is represented by a dashed blue line.

this instance, the mode matching assigned a higher likelihood value than was appropriate. As a result, the algorithm's convergence slowed[10].

Second, inferring only two stiffness parameters for all the frame levels may have been insufficient, preventing the model from producing frequencies with higher likelihood. For instance, the updated FEM output produced frequencies that were compensated, with an average error across all frequencies of 0.42%. This may indicate that any modification on a stiffness parameter will increase or decrease all frequencies, without reducing the average error.

Third, the posterior PDF of the uncertainty variable σ (denoted as θ_5) is concentrated near the upper bound of its interval, suggesting that a higher upper limit should be considered. Nevertheless, the values of σ would probably be lower if the likelihood were correctly computed and the model were more accurate.

These insights are crucial for the next Bayesian inference, which will consider both frequencies and mode shapes. First, the mode matching process must be refined[11]. Second, the model should be improved by increasing the number of uncertainty stiffness parameters. These considerations will be accounted for in future work.

[10]In fact, the selected burn-in period may be too short, as the log-likelihood expectation curve had not yet leveled off at that point.

[11]One possible approach is to identify two clusters: x-bending modes and the torsional mode. Once the modes are grouped, the matching becomes straightforward, as there is only one torsional mode, and the x-bending modes can be matched by ordering them according to their increasing frequency.

3.2. Steel Footbridge

3.2.1. Description of the Structure

The second case study involves a real steel truss footbridge located at P.K. 121/835 on the Bobadilla-Granada Railway, in Granada. The structure was built in 2003 by the Ayuntamiento de Granada, and connects La Rosaleda and La Chana neighbourhoods by crossing the aforementioned High Speed Railway.

The choice of this structure as a case study is justified by its nature as a steel structure, the opportunity to study its joints, the peculiarity of its dynamics, and its easy access. A photo of the structure is shown in Figure 3.17.

Figure 3.17: Case study 2: steel footbridge.

The central part of the footbridge is a Warren truss of 2.45 m and 18.57 m length, supported by 2 piles of 6.79 m height. Access to the central lattice is provided by ramps and stairs, both of which have a free width of 1.38 m. The ramp has a total length of 67.5 meters, while the stairs consist of 33 steps. The plan view of the footbridge is shown in Figure 3.18, and the ramp plan is depicted in Figure 3.19.

The materials used are A-42 steel[12], which is used for the entire structure, and H-25 reinforced concrete[13], which is used for the pile foundations and the footbridge pavement. The steel bars used are B500S, and have diameters ranging from 8 to 32 mm.

The most critical part for the structure safety is the central Warren truss, which is the focus of the monitoring system to be deployed. Nevertheless, its dynamics is completely conditioned by the ramps and stairs that allow to access to it. Indeed, the two main piles of the structure support all three elements (central truss, ramps and stairs) and consequently connect their vibration.

3.2.2. Monitoring System

The monitoring of the structure has not yet been carried out due to the lack of necessary equipment, particularly the power station, which could not be acquired within

[12] According to the convention used in NBE-EA-95, corresponding to a yield strength of 260 MPa.

[13] According to the convention used in EHE-98, corresponding to a C25/30 in Eurocode 2.

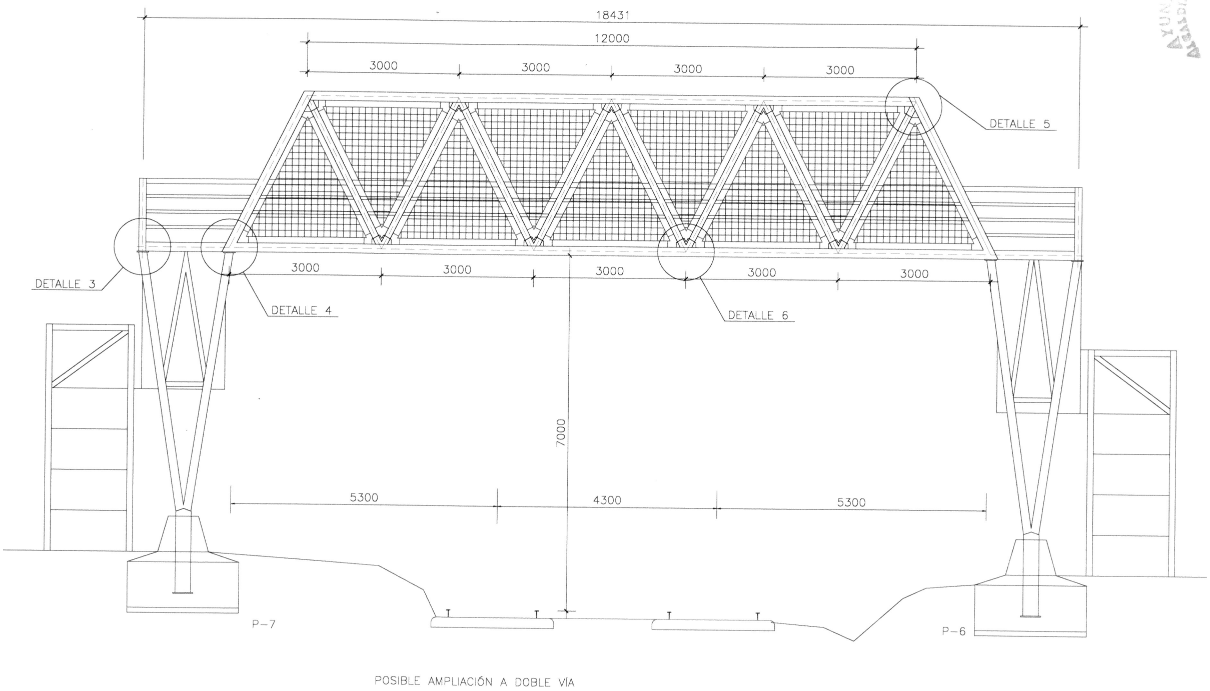

Figure 3.18: Plan view of the steel footbridge.

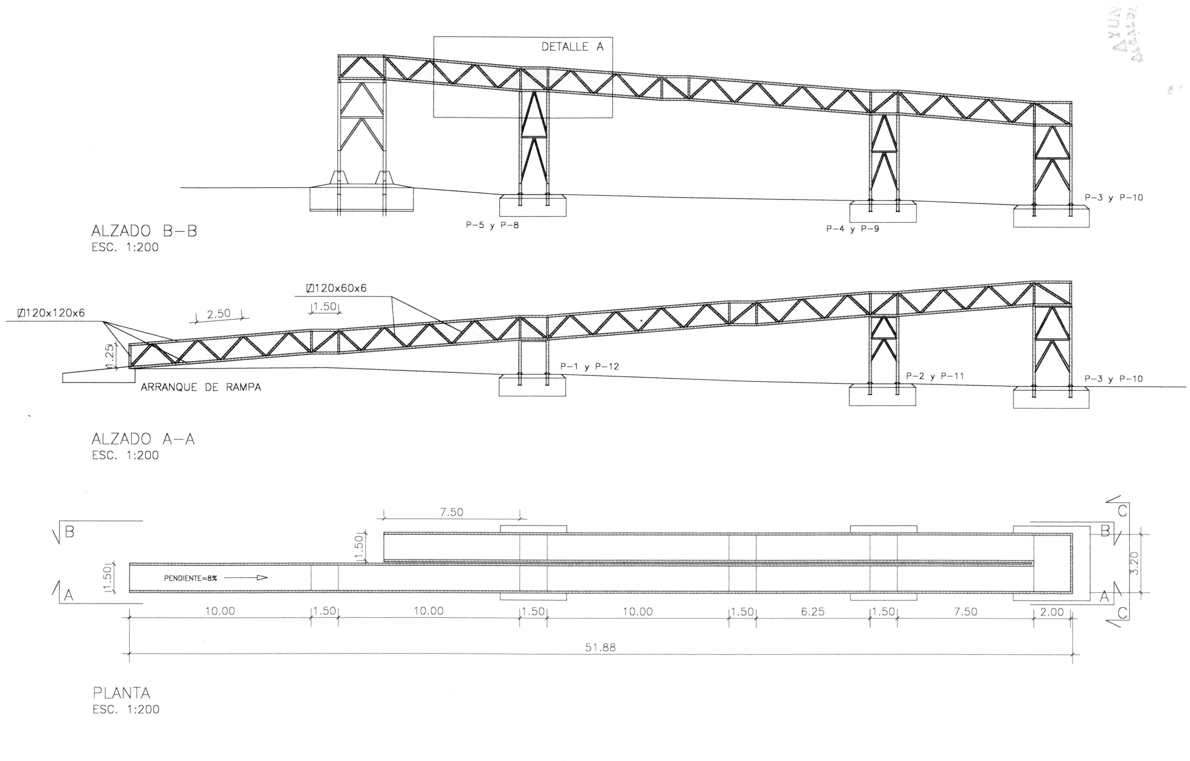

Figure 3.19: Access ramp plan.

the required time frame because of bureaucratic challenges.

To address this limitation, simulated time-history strain data was obtained from the FEM, as detailed in Section 3.2.4. The strain data was collected from 13 points of the model, corresponding to 13 simulated SGs. Their locations are shown in Figure 3.20, where the position of the SGs is indicated by arrows perpendicular to the surface of the element on which they are placed. The exact coordinates of the simulated SGs are summarized in Table 3.6.

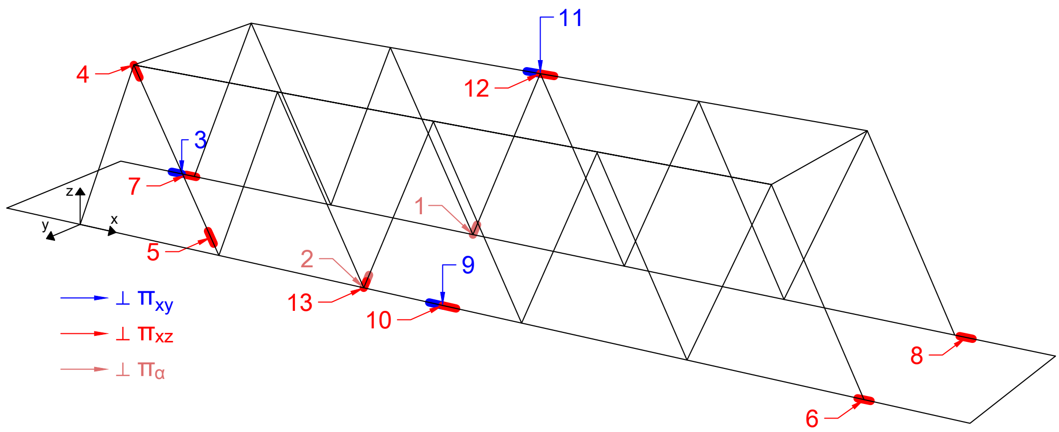

Figure 3.20: Locations of the SGs on the footbridge. Locations are indicated by arrows perpendicular to the surface of the element on which they are placed. Blue arrows are perpendicular to the x-y plane (π_{xy}), red arrows are perpendicular to the x-z plane (π_{xz}), and green arrows are perpendicular to the π_α plane, which is defined by the directions of the upright on which they are placed and the x-axis.

Table 3.6: SGs location - footbridge

Channel	x (m)	y (m)	z (m)	Monitored element
1	6.000	2.800	0.000	Upright
2	6.000	0.000	0.000	Upright
3	-0.280	2.800	0.000	Lower chord
4	1.500	0.000	3.000	Upright
5	2.850	0.000	0.300	Upright
6	15.000	0.000	0.000	Lower chord
7	-0.194	2.800	0.000	Lower chord
8	15.194	2.800	0.000	Lower chord
9	7.500	0.000	0.000	Lower chord
10	7.500	0.000	0.000	Lower chord
11	7.500	2.800	3.000	Upper chord
12	7.500	2.800	3.000	Upper chord
13	6.000	0.000	0.000	Upright

The real monitoring campaign is scheduled for September, for which the structure is proposed to be monitored with 8 SGs. These correspond to the EfI optimal configuration for six target mode shapes, as described in Section 3.2.3.

3.2.3. FEM and OSP Scheme

A FEM of the footbridge has been developed using *SAP2000* software. A general view is depicted in Figures 3.21 and 3.22.

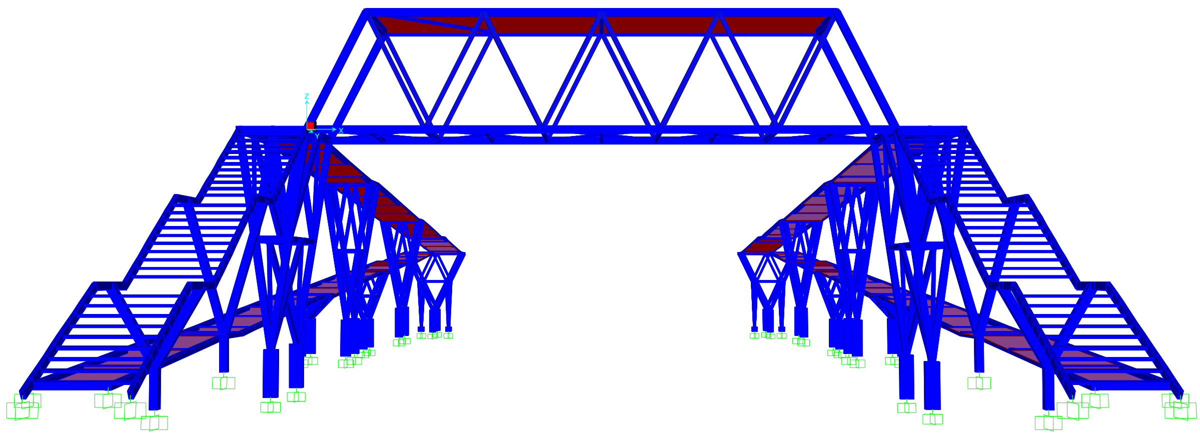

Figure 3.21: Footbridge FEM. Front view.

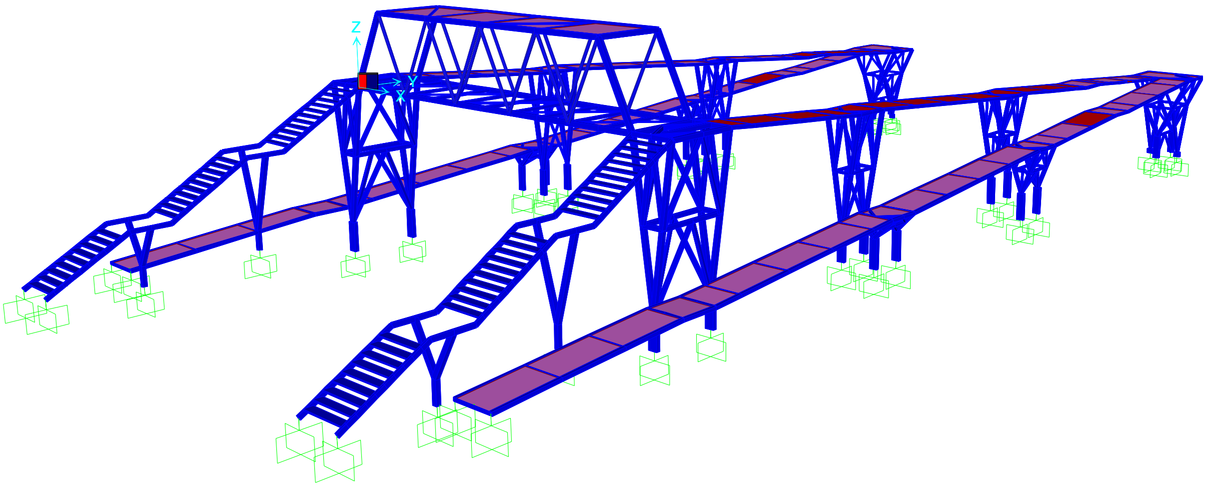

Figure 3.22: Footbridge FEM. General view.

As previously discussed, the central Warren truss is coupled with the rest of the elements in the bridge through the piles. This coupling means that the dynamics of this main part of the bridge cannot be analyzed independently, so all bridge elements have been modelled.

Two types of elements have been used in the model: 2-D area objects and 1-D frame objects.

2-D elements have been introduced to link individual components and remove local modes of vibration. Specifically:

- An area object has been introduced in the ceiling of the Warren truss, modeling the profiled sheet metal that physically exists.

- An area object has been introduced to model the concrete pavement of ramps, thus removing the local modes associated with the vibration of the ramp elements.

The 1-D frame sections used in each footbridge part are:

- **Central Warren truss**:
  - Bottom and upper chords: rectangular hollow section modeling 2-UPN-180 profiles.
  - Uprights: circular hollow section 125.5.
  - Elements connecting chords in the horizontal plane: rectangular hollow section modeling 2-UPN-100 profiles, and angular profiles 60.60.6.
- **Piles**: The following rectangular hollow sections have been used: 60.160.10, 90.90.6, 90.160.6, 90.160.10, 120.60.6, 120.120.6, 140.140.6, 160.160.10, 160.360.10, 320.140.10.
- **Stairs**: Rectangular hollow section modeling 2-UPN-160 profiles and rectangular section 300.45 for the steps (necessary to remove local modes).
- **Ramps**: 2-D Warren truss constituting the ramps rail have been modeled with equivalent Timoshenko beams (as explained below). Additionally, the following rectangular hollow sections 90.50.6 and 120.120.6 are defined to connect the equivalent beams in the horizontal plane (and so, avoid calculating local modes).

As mentioned earlier, the 2-D Warren truss constituting the stairs rails has been modeled with an equivalent Timoshenko beam, thus avoiding the calculation of some local modes associated to these two dimensional elements. A procedure to calculate such an equivalent beam has been developed, its derivation being detailed in Appendix II. In this section, only the results are provided.

Considering a Warren truss like the one shown in Figure 3.23, the properties of the equivalent Timoshenko beam are as follows: the equivalent linear density is provided by Equation (3.11), the equivalent inertia for in-plane bending is given by Equation (3.12), and the equivalent shear area is defined by Equation (3.13).

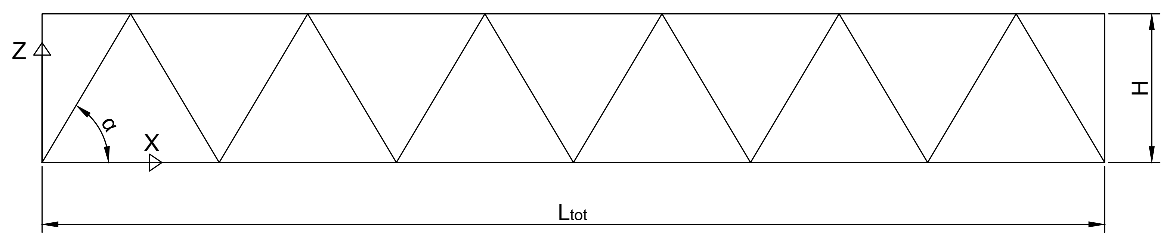

Figure 3.23: Geometric characteristics of Warren truss.

$$\rho_L^{\mathrm{eq}} = \left(\frac{2\left(L_{\mathrm{tot}} + H\right) + \frac{L_{\mathrm{tot}}}{\cos(\alpha)}}{L_{\mathrm{tot}}} \right) \rho_L \tag{3.11}$$

$$I_y^{\mathrm{eq}} = 2\left(I_y + \left(\frac{H}{2}\right)^2 A \right) \tag{3.12}$$

$$A_c^{\mathrm{eq}} = 2(1+\nu)A\sin^2(\alpha)\cos(\alpha) \tag{3.13}$$

where:

- ν, A, I_y, and ρ_L represent the Poisson's ratio, cross-sectional area, in-plane moment of inertia, and linear density of the truss elements, respectively. It is assumed that all elements (uprights, upper and lower chords) have the same section, as is the case for the footbridge.

- L_{tot}, H, and α denote the total length of the Warren truss, its height (or distance between the lower and upper directrices), and the positive angle between the uprights and the upper and lower chords, respectively.

The complexity of the structure's dynamics is reflected in the mode shapes that jointly affect the ramps, stairs, piles, and the central Warren truss. Since the monitoring excludes the ramps and stairs, only the mode shapes related to the central Warren truss are considered as target modes. Consequently, mode shapes such as the one shown in Figure 3.24 are excluded from the target modes of the EfI algorithm.

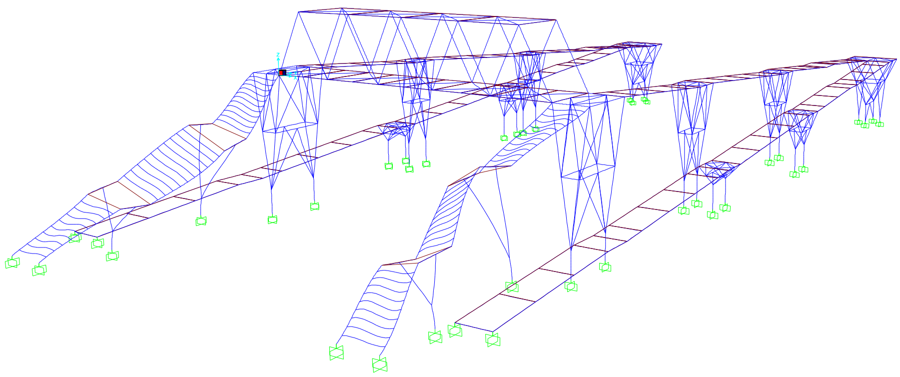

Figure 3.24: Example of mode shape non-considered as target mode for EfI (mode 5).

The identification of these mode shapes is challenging due to the aforementioned complexity. To facilitate this process, a simplified FEM, focusing solely on the central Warren truss and its piles, has been used to help identify the target mode shapes[14]. The EfI algorithm was applied to the full FEM.

Target mode shapes considered for the EfI algorithm are summarized in Table 3.7 and illustrated in Figure 3.25, where the ramps and the stairs have been removed from the view for clarity.

The EfI algorithm was applied to determine the OSP of the SGs, taking into account that only the main elements of the central Warren truss (uprights, upper and lower chords) are accessible. Consequently, the candidate DOFs are the mesh points of those elements in the FEM model (12 equally-distributed points per element). The number of sensors must satisfy the condition $l \geq m$. A good balance between using fewer sensors and achieving higher linear independence of the modes (assessed by the lowest value of the E_D vector; see Figure 3.26) was found with eight SGs.

[14] Not surprisingly, the frequencies in the simplified model are considerably lower than those in the full FEM, since the contribution of the rest of the structure to the overall stiffness is excluded.

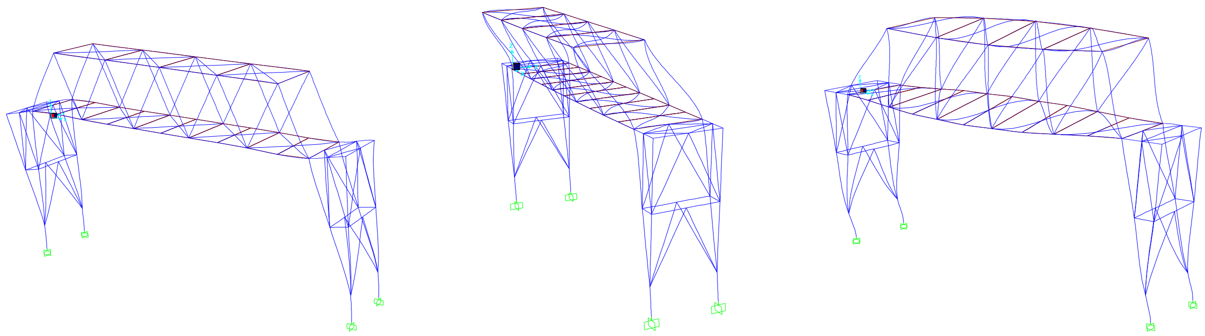

(a) Mode 1. (b) Mode 4. (c) Mode 15.

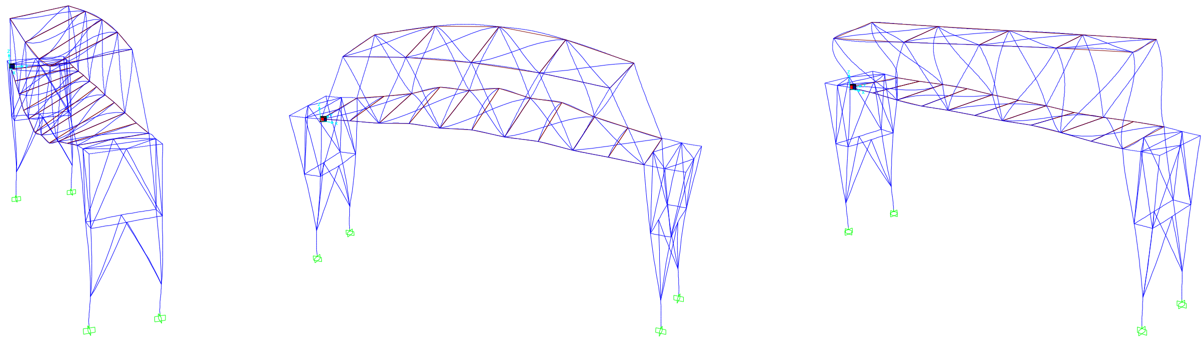

(d) Mode 27. (e) Mode 28. (f) Mode 38.

Figure 3.25: Footbridge: target mode shapes for EfI algorithm.

Table 3.7: Considered mode shapes for EfI algorithm - footbridge

Mode Number	Frequency (Hz)	Type of Mode
1	2.692	First bending mode of piles (weak axis)
4	5.449	First Warren truss horizontal bending mode
15	11.579	First bending mode of piles (strong axis)
27	15.177	First torsional mode
28	15.368	First Warren truss vertical bending mode
38	20.389	Second Warren truss horizontal bending mode

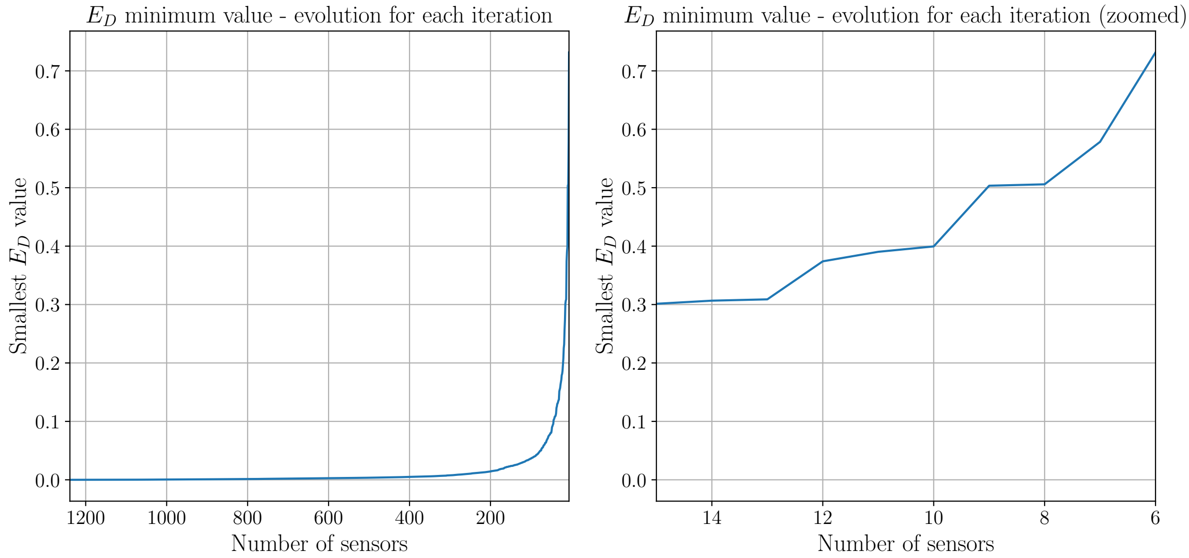

Figure 3.26: EfI Algorithm - E_D evolution for each iteration.

The SGs optimal locations obtained with the EfI algorithm are shown in Figure 3.27a, where the position of the SGs is indicated by arrows perpendicular to the surface of the element on which they are placed. For clarity, only the frames containing candidate DOFs are shown.

The exact locations of these sensors correspond to channels 1 to 8 of Table 3.6.

3.2.4. OMA Results

A simulated Operational Modal Analysis (OMA) was conducted with two main objectives: to gain insights for the upcoming real monitoring campaign and to evaluate the effectiveness of the EfI-based OSP configuration. In the absence of real data, dynamic strain measurements were generated through a time history analysis in *SAP2000*, using ground motion as the excitation source. A constant damping rate of $\xi_k = 2\%$ was assumed for all modes $(k = 1, \ldots, m)$.

The characteristics of the test are as follows:

- Sampling frequency: $f_s = 50$ Hz.
- Excitation force: white noise acceleration applied in three directions at the structure's supports
- Test duration: 5 minutes. According to the well-known rule of 2000 times the fundamental period T_1, the recommended duration would be approximately 12 minutes and 35 seconds. However, due to the high memory consumption of time history analysis in *SAP2000*, the analysis duration was shortened.
- Sensor layout: 13 SGs (locations shown in Figure 3.20), corresponding to two different configurations: the EfI Optimal Scheme described in 3.2.3 (Figure 3.27a) and an additional sub-optimal configuration (Scheme B, shown in Figure 3.27b). Scheme B includes three channels from Scheme A and five additional channels selected based

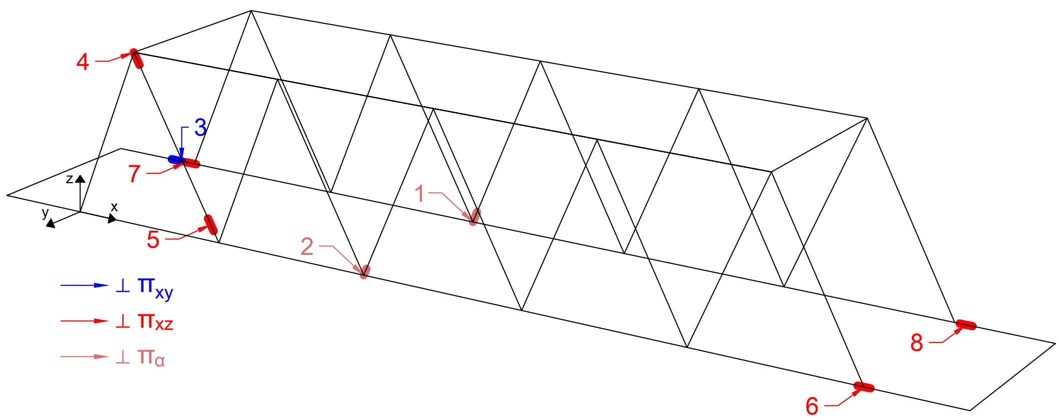

(a) SGs in Scheme A.

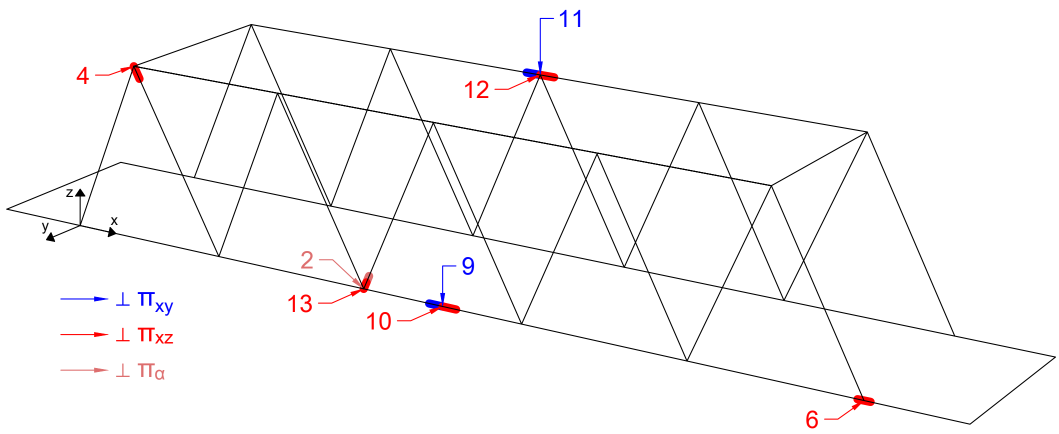

(b) SGs in Scheme B.

Figure 3.27: Footbridge: SGs schemes. The location of the SGs is indicated by arrows perpendicular to the surface of the element on which they are placed. Blue arrows are perpendicular to the x-y plane (π_{xy}), red arrows are perpendicular to the x-z plane (π_{xz}), and green arrows are perpendicular to the π_α plane, which is defined by the directions of the upright on which they are placed and the x-axis.

on engineering judgment. The channels for each scheme are listed in Table 3.8, and the coordinates of each channel are specified in Table 3.6.

Table 3.8: Selected channels for each configuration - footbridge

Scheme A (EfI-Optimal)	**Scheme B (Sub-optimal)**
1	2
2	4
3	6
4	9
5	10
6	11
7	12
8	13

The EFDD algorithm was used to perform OMA on the simulated dynamic strain data. The SVP of the thirteen channels is illustrated in Figure 3.28.

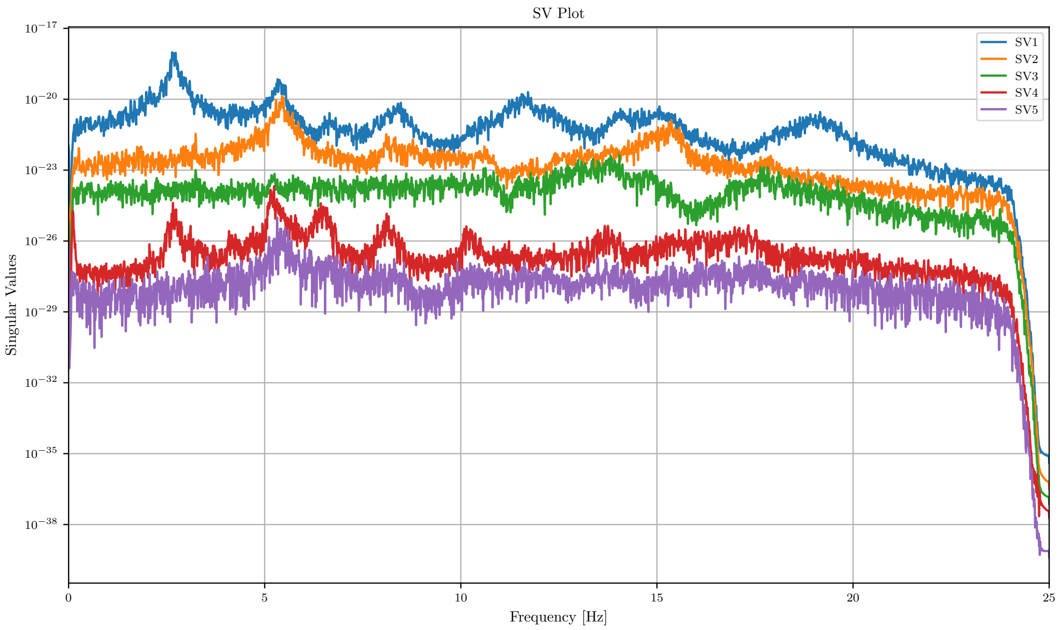

Figure 3.28: SVP for all channels.

It can be observed that, among the six target modes, only the first five were identified. Additionally, other non-target modes are also identifiable in the SVP, as discussed later.

The frequencies of vibration, identified as peaks in the SVP, are detailed in Table 3.9. It is worth noting that the fifth mode has been identified in the second singular value. The strain mode shape coordinates for the two schemes are presented in Appendix I.

The comparison of the strain mode shapes linear independence between the two SGs configurations is made through the AutoMAC matrix, defined in equation (2.36). A graphical representation of the two AutoMAC matrices is depicted in Figure 3.29.

Table 3.10 collects the off-diagonal mean and highest values for the two AutoMAC matrices. It is observed from Figure 3.29a and from Table 3.4 that the Scheme A,

Table 3.9: Frequencies of vibration from OMA - footbridge

Mode Number	Frequency (Hz)	Type of Mode
1	2.654	First bending mode of piles (weak axis)
2	5.444	First Warren truss horizontal bending mode
3	11.616	First bending mode of piles (strong axis)
4	15.340	First torsional mode
5	15.354	First Warren truss vertical bending mode

corresponding to the EfI configuration, produces the best results, thus experimentally proving the effectiveness of this algorithm.

Table 3.10: Off-diagonal metrics for schemes A and B - footbridge

	Off-diagonal mean value	**Off-diagonal highest value**
Scheme A	0.063	0.369
Scheme B	0.138	0.617

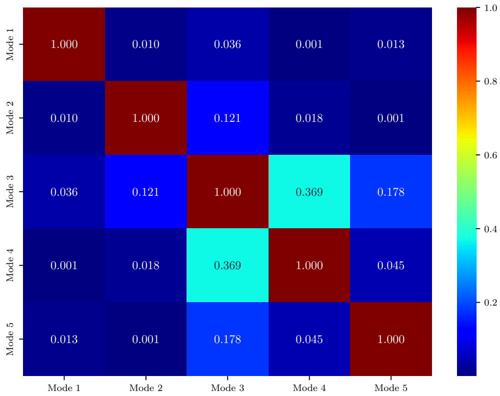

(a) AutoMAC Scheme A.

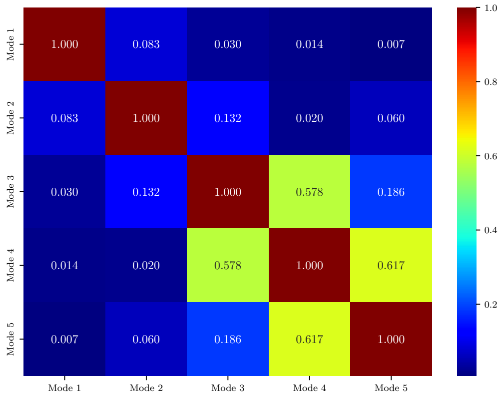

(b) AutoMAC Scheme B.

Figure 3.29: Comparison of the AutoMAC matrices for two configuration schemes.

The results obtained from this simulated OMA provide valuable insights for the upcoming real monitoring campaign. First, additional modes beyond those originally considered as target modes have been identified. This includes a second mode closely spaced to the one at 5.444 Hz (which can be observed in the second singular value), a mode at 8.370 Hz, and another at 19.172 Hz. All of these are visible in the SVP shown in Figure 3.28. Additionally, the mode at 20.389 Hz is not observable.

These observations may prompt a reconsideration of the target mode shapes and the placement of the SGs.

Chapter 4

Conclusions and Future Works

4.1. Conclusions

The project successfully implemented the full monitoring cycle on a laboratory-scale steel frame structure. This cycle included the following key steps:

1. Generating a FEM of the structure.
2. Calculating optimal sensor locations.
3. Assembling electronic components for data acquisition.
4. Recording structural vibrations.
5. Performing OMA.
6. Utilizing modal data for inferring model parameters.

While the full process was completed for the laboratory structure, the same steps—except for model updating—were also applied to a real pedestrian footbridge. In this case, the lack of real data was addressed using simulated strain vibration data.

From a practical standpoint, the works carried out in this project have yielded valuable outcomes. The Python codes developed, along with the hands-on experience gained, will significantly facilitate the monitoring of real structures in future campaigns.

From a research perspective, this project addresses the EfI method to real structures using SGs, which was a gap identified in the literature. The EfI has demonstrated its effectiveness by producing mode shapes with higher linear independence compared to those obtained through traditional engineering sensor location. This advancement validates the potential of strain-based monitoring for enhancing structural health monitoring systems.

The work conducted on the footbridge, despite relying on simulated data, has provided crucial insights. These findings will enhance the effectiveness of the upcoming real monitoring campaign.

4.2. Future Works

Future work on the steel frame will focus on performing Bayesian Inference using all modal parameters (frequencies and strain mode shapes) and adding more variables to the model parameters[1]. An important step will be to implement an enhance mode matching

[1] For instance, using different ending stiffness of the connecting frames for each frame level.

method, as discussed in Section 3.1.5. Furthermore, the impact of the EfI algorithm on the inferred parameters will be assessed. To improve computational efficiency, the development of a surrogate model will also be considered, to enable faster Bayesian inference.

Regarding the footbridge, the next steps will involve conducting a real OMA, followed by FEM updating using Bayesian Inference. The monitoring system configuration may be reconsidered based on the findings from the simulated results, particularly regarding the target modes. Moreover, additional aspects such as model sub-structuring will be explored, given the dynamic behavior of the footbridge.

As a continuation of this work, we are currently in the process of organizing and refining the results obtained for submission to a scientific journal.

Appendix I: OMA Results

A.I.1. Strain Mode Shapes for Steel Frame

Table A.I.1: Scheme A: strain mode shapes using EFDD - Steel Frame

SG \ Mode	1	2	3	4	5	6
3	-0.790+0.000j	-1.000-0.000j	-0.769+0.000j	-0.833-0.000j	-0.581-0.000j	-0.988+0.000j
4	-0.955-0.007j	-0.520+0.184j	0.895+0.013j	0.704+0.033j	-0.553-0.118j	-0.208-0.042j
7	-0.266-0.011j	0.129-0.201j	-0.747-0.051j	1.000+0.090j	1.000+0.233j	-0.978+0.052j
8	0.503-0.012j	-0.278+0.212j	1.000-0.112j	-0.474+0.104j	0.442+0.037j	-0.987+0.293j
9	0.451+0.016j	0.791+0.143j	0.992+0.122j	-0.441-0.050j	0.359+0.211j	-1.000-0.157j
11	-0.815-0.050j	0.619-0.113j	-0.730-0.089j	-0.774-0.207j	-0.555-0.205j	-0.923-0.296j
14	-0.921-0.044j	-0.567+0.029j	0.161+0.018j	-0.589-0.126j	0.796+0.370j	0.500+0.205j
15	-1.000-0.105j	0.859+0.096j	0.193+0.087j	-0.565-0.282j	0.700+0.666j	0.436+0.402j

Table A.I.2: Scheme B: strain mode shapes using EFDD - Steel Frame

SG \ Mode	1	2	3	4	5	6
2	-0.565-0.000j	0.853+0.000j	-0.646+0.000j	-0.911+0.000j	-0.971-0.000j	-0.977-0.000j
3	-0.611-0.031j	-1.000-0.590j	-0.746-0.165j	-1.000-0.284j	-1.000-0.358j	-1.000-0.436j
4	-0.740-0.043j	-0.671-0.166j	0.871+0.216j	0.832+0.282j	-0.867-0.524j	-0.210-0.153j
10	-0.953-0.120j	0.536+0.603j	0.986+0.485j	0.739+0.539j	-0.572-0.758j	-0.131-0.239j
11	-0.629-0.071j	0.763+0.279j	-0.697-0.250j	-0.862-0.511j	-0.830-0.695j	-0.802-0.732j
12	-0.568-0.081j	0.643+0.513j	0.663+0.361j	0.521+0.413j	-0.401-0.673j	-0.102-0.170j
16	-0.629-0.088j	-0.595-0.628j	-0.698-0.382j	-0.751-0.671j	-0.617-0.863j	-0.537-0.944j
17	-1.000-0.109j	-0.924-0.321j	1.000+0.421j	0.793+0.514j	-0.610-0.746j	-0.151-0.191j

Table A.I.3: Scheme C: strain mode shapes using EFDD - Steel Frame

SG \ Mode	1	2	3	4	5	6
1	-0.714+0.000j	-0.985-0.000j	-0.251-0.000j	-0.739+0.000j	-1.000+0.000j	-0.626+0.000j
2	-0.589+0.026j	-0.732+0.382j	0.569-0.153j	-0.957+0.172j	0.514-0.203j	0.831-0.283j
8	0.407-0.007j	0.391-0.253j	-0.915+0.139j	-0.652+0.075j	-0.465-0.012j	1.000-0.207j
10	-1.000-0.081j	-0.717-0.348j	-1.000-0.198j	0.884+0.434j	0.475+0.288j	0.179+0.154j
11	-0.660-0.045j	-0.777+0.062j	0.675+0.056j	-1.000-0.377j	0.580+0.190j	0.898+0.392j
12	-0.596-0.058j	-0.753-0.237j	-0.683-0.164j	0.629+0.338j	0.364+0.281j	0.140+0.124j
13	0.384+0.036j	0.458-0.090j	-0.889-0.173j	-0.617-0.272j	-0.343-0.281j	0.924+0.580j
15	-0.809-0.090j	-1.000-0.176j	-0.182-0.073j	-0.717-0.453j	-0.769-0.667j	-0.403-0.430j

A.I.2. Strain Mode Shapes for Footbridge

Note in the tables below that the mode shapes are reported in complex form, as outputted by the EFDD algorithm. Nevertheless, it can be readily seen that the modal components are aligned (real mode shapes), as it is expected since proportional damping was defined in the *SAP2000* model.

Table A.I.4: Scheme A: strain mode shapes using EFDD - footbridge

SG \ Mode	1	2	3	4	5
1	0.014+0.002j	-0.087-0.026j	-0.957-0.075j	-0.255-0.062j	-1.000-0.216j
2	0.042+0.020j	0.093+0.027j	1.000+0.037j	1.000+0.449j	-0.379-0.098j
3	1.000+0.348j	0.019+0.005j	0.333+0.019j	-0.016-0.000j	0.210+0.103j
4	-0.165-0.062j	1.000+0.319j	-0.851-0.226j	0.031+0.009j	-0.086-0.017j
5	0.053+0.026j	0.025+0.003j	0.261+0.016j	0.574+0.030j	-0.254-0.078j
6	-0.472-0.068j	-0.023-0.000j	0.148+0.071j	-0.017-0.008j	0.020+0.004j
7	-0.480-0.118j	-0.021-0.004j	-0.510-0.191j	0.034+0.008j	-0.238-0.027j
8	0.439+0.052j	-0.017-0.007j	-0.534-0.233j	0.036+0.010j	-0.248-0.107j

Table A.I.5: Scheme B: strain mode shapes using EFDD - footbridge

SG \ Mode	1	2	3	4	5
2	0.088+0.042j	0.093+0.027j	1.000+0.037j	1.000+0.449j	-1.000-0.257j
4	-0.350-0.131j	1.000+0.319j	-0.851-0.226j	0.031+0.009j	-0.227-0.045j
6	-1.000-0.144j	-0.023-0.000j	0.148+0.071j	-0.017-0.008j	0.054+0.009j
9	-0.000-0.000j	0.039+0.001j	0.397+0.022j	-0.104-0.028j	0.291+0.062j
10	-0.000-0.000j	0.039+0.011j	0.397+0.009j	-0.104-0.010j	0.291+0.077j
11	-0.000-0.000j	-0.031-0.015j	0.184+0.070j	0.087+0.002j	0.641+0.092j
12	-0.000-0.000j	-0.031-0.007j	0.184+0.027j	0.087+0.029j	0.641+0.277j
13	0.088+0.002j	0.093+0.032j	1.000+0.021j	1.000+0.403j	-1.000-0.381j

Appendix II: Timoshenko beam equivalent of the Warren truss

A.II.1. Mathematical Formulation

Let us consider a Warren truss with the following parameters (see Figure A.II.1):

- Geometrical characteristics:
  - L_{tot}: Total length of the truss.
  - H: Distance between the upper and lower directrices.
  - α: Positive angle between the uprights and the upper and lower chords.
  - L_{up}: Lenght of the uprights; $L_{\text{up}} = \frac{H}{\sin(\alpha)}$
  - d: Distance between joints; $d = \frac{2H}{\tan(\alpha)}$
  - n: Number of internal joints in the lower chord; $n = \frac{L_{\text{tot}}}{d} - 1$
- Section characteristics[2]: Bernoulli-Euler elements are considered, with the following characteristics:
  - A: Cross-sectional area of the elements.
  - I_y: Inertia for in-plane bending.

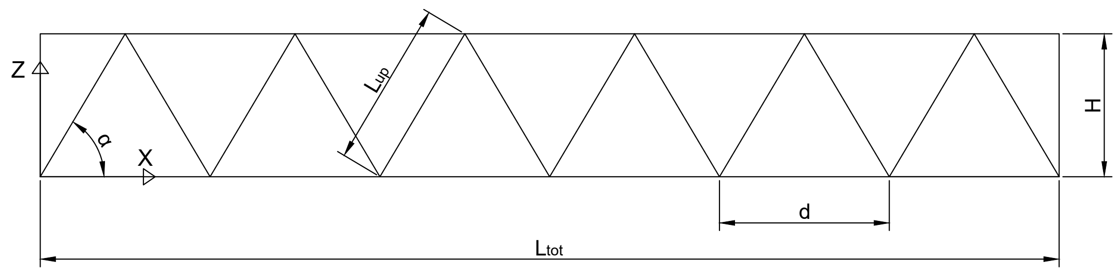

Figure A.II.1: Geometric characteristics of Warren truss.

The problem consists of defining an equivalent 1-D Timoshenko beam with the same length (L_{tot}) such that its in-plane bending dynamic properties are equivalent to those of the 2-D Warren truss.

[2]Uprights, lower chord, and upper chord are assumed to have the same cross-sectional area, as is the case in the footbridge. However, the formulation can be easily generalized for different sections.

The in-plane dynamic characteristics of a Timoshenko beam are dominated by the equivalent linear density (ρ_L^{eq}), the equivalent in-plane moment of inertia (I_y^{eq}), and the equivalent shear area (A_c^{eq}).

Equivalent Linear Density (ρ_L^{eq}):

The equivalent linear density is calculated such that the equivalent Timoshenko beam has the same mass as the Warren truss. The mass of the Warren truss is given by:

$$m = \rho_L \left(2\left(L_{\mathrm{tot}} + H\right) + 2(n+1)L_{\mathrm{up}}\right) = \rho_L \left(2\left(L_{\mathrm{tot}} + H\right) + \frac{L_{\mathrm{tot}}}{\cos(\alpha)}\right) \tag{A.II.1}$$

The mass of the equivalent Timoshenko beam is given by:

$$m^{\mathrm{eq}} = \rho_L^{\mathrm{eq}} L_{\mathrm{tot}} \tag{A.II.2}$$

By equating (A.II.1) and (A.II.2), the equivalent linear density is determined as follows:

$$\rho_L^{\mathrm{eq}} = \left(\frac{2\left(L_{\mathrm{tot}} + H\right) + \frac{L_{\mathrm{tot}}}{\cos(\alpha)}}{L_{\mathrm{tot}}}\right)\rho_L \tag{A.II.3}$$

Equivalent Moment of Inertia for In-Plane Bending (I_y^{eq}):

The Warren truss is assumed to behave as a beam with a section formed by the lower and upper chords, which are spaced by a distance H. Consequently, the moment of inertia for in-plane bending of this equivalent beam is given by:

$$I_y^{\mathrm{eq}} = 2\left(I_y + \left(\frac{H}{2}\right)^2 A\right) \tag{A.II.4}$$

Equivalent shear area (A_c^{eq}):

The equivalent Timoshenko beam accounts for displacements due to axial forces in the uprights as a shear deformation, modulated by the shear area. Let us consider a load case consisting in vertical loads applied at the n internal joints of the lower chord, as shown in Figure A.II.2. The equivalent shear area A_c^{eq} is defined such that the shear deformation due to this load case equates the deformation of the Warren truss resulting from the axial strain in the uprights.

The axial force supported by the uprights is given by the following expressions:

$$N_{i,1} = -\frac{P(n-2i)}{2\sin(\alpha)}, \quad N_{i,2} = \frac{P(n-2i)}{2\sin(\alpha)}, \quad \text{for } i = 0, \ldots, n \tag{A.II.5}$$

where the following convention has been used: i refers to the uprights between joint i and $i+1$, with $i = 0, \ldots, n$;1 refers to the first upright (starting from the left), and 2 refers to the second upright.

The vertical displacement (considered positive when downwards) in each upright is given by[3]:

[3]Assuming small displacements.

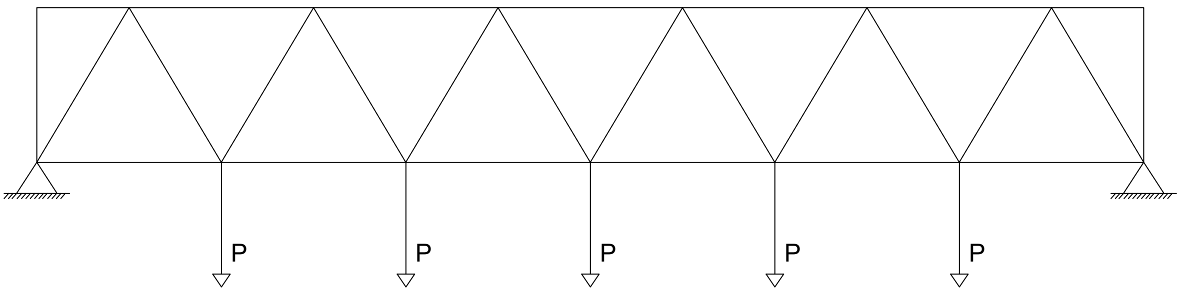

Figure A.II.2:]
Load case of Warren truss.

$$\Delta w_{i,j} = -\frac{N_{i,j} L_{\text{up}}}{EA \sin(\alpha)} \quad \text{with } i = 0, \ldots, n;\ j = \{1, 2\}. \tag{A.II.6}$$

So the (accumulated) vertical deflection in joint k is given by

$$w_k = w(k \cdot d) = \sum_{i=0}^{k-1} \sum_{j=1}^{2} \Delta V_{i,j} = \sum_{i=0}^{k-1} \frac{P(n-2i) L_{\text{up}}}{EA \sin^2(\alpha)} \tag{A.II.7}$$

For the equivalent Timoshenko beam, the vertical displacement is:

$$w^{\text{eq}}(x) = \frac{1}{GA_c} \int_0^x V(t)\, dt \tag{A.II.8}$$

Where $V(t)$ is the shear force. Considering that for the assumed load case, $V(t)$ is piece-wise constant between joints,

$$w^{\text{eq}}(x_k) = w^{\text{eq}}(k \cdot d) = \frac{d}{GA_c} \sum_{i=0}^{k-1} \frac{V_i}{2} = \frac{d}{GA_c} \sum_{i=0}^{k-1} \frac{P(n-2i)}{2}. \tag{A.II.9}$$

By equating (A.II.7) and (A.II.9), the expression for A_c is:

$$A_c = \frac{EA \sin^2(\alpha) \cdot d}{2GL_{\text{up}}} \tag{A.II.10}$$

Finally, substituting $G = \frac{E}{2(1+\nu)}$, $d = \frac{2H}{\tan(\alpha)}$, and $L_{\text{up}} = \frac{H}{\sin(\alpha)}$ into Equation (A.II.10), the following expression for the shear area of the equivalent Timoshenko beam is obtained:

$$A_c = 2(1+\nu) A \sin^2(\alpha) \cos(\alpha). \tag{A.II.11}$$

The equations (A.II.3), (A.II.4), and (A.II.11) are the same expressions provided in (3.11), (3.12), and (3.13).

A.II.2. FEM Validation

To validate the developed formulation, two numerical examples are calculated: Example 1 (short truss) and Example 2 (Long truss). The Warren truss geometrical characteristics are shown in Table A.II.1:

The frequencies for the first 2 modes of vibration in Example 1 (there is not a pure bending third mode), and 3 modes of vibration in Example 2 have been calculated with

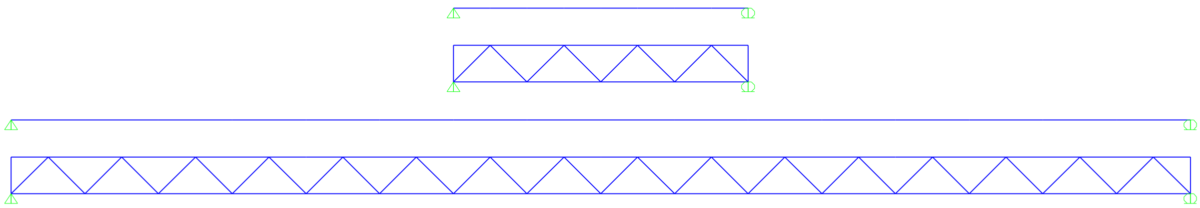

Figure A.II.3: *SAP2000* models for Example 1 (upper elements) and Example 2 (bottom elements). The linear depicted are used to compute the frequencies of the equivalent Bernoulli-Euler and Timoshenko beams.

Table A.II.1: Geometrical parameters for the two examples

	H (m)	L_{tot} (m)	α (degrees)
Example 1	1.25	10	45
Example 2	1.25	40	45

SAP2000. The results include the values for the 2-D truss, for the equivalent Timoshenko beam and for the Equivalent Bernoulli-Euler beam (which does not account for the shear deformation).

The values are gathered in Table A.II.3 and Table A.II.2. It can be seen that the results are acceptable, and that including the effect of the shear deformation enhances the accuracy.

Table A.II.2: Vibration mode frequencies (Hz) for Example 1

	2D Truss	**BE-Equiv**	**Timoshenko-Equiv**
Mode 1	37.62	33.04	34.03
Mode 2	150.42	77.88	108.47

Table A.II.3: Vibration mode frequencies (Hz) for Example 2

	2D Truss	**BE-Equiv**	**Timoshenko-Equiv**
Mode 1	2.35	2.41	2.34
Mode 2	9.4	9.33	9.15
Mode 3	21.16	19.4	19.93

Bibliography

[1] Cesar A. Calderon and Luis Servén. The effects of infrastructure development on growth and income distribution. World Bank Policy Research Working Paper 3400, World Bank, Washington DC, 2004.

[2] European Investment Bank. *Better infrastructure, better economy.* European Investment Bank, 2016.

[3] Gelsomina Catalano and Davide Sartori. Infrastructure investment long term contribution: Economic development and wellbeing. Working Papers 201301, CSIL Centre for Industrial Studies, March 2013.

[4] European Investment Bank. *Investment Report 2021/2022: Recovery as a springboard for change.* European Investment Bank, Luxembourg, 2022.

[5] Björn Åkesson. *Understanding Bridge Collapses.* CRC Press, Taylor & Francis, London, UK, 1st edition edition, 2008. eBook published 21 April 2014.

[6] American Road and Transportation Builders Association. Bridge report, 2020. Technical report, American Road & Transportation Builders Association, 2020.

[7] Konstantinos Gkoumas, Fabio Marques Dos Santos, Mitchell Van Balen, Anastasios Tsakalidis, Alejandro Ortega Hortelano, Monica Grosso, Anwar Haq, and Ferenc Pekar. Research and innovation in bridge maintenance, inspection and monitoring. Science for policy, Energy and transport, Safety and security EUR 29650 EN, Publications Office of the European Union, Luxembourg, 2019. JRC115319.

[8] John Besant-Jones, Antonio Estache, Gregory K. Ingram, Christine Kessides, Peter Lanjouw, Ashoka Mody, and Lant Pritchett. *World Development Report 1994: Infrastructure for Development.* World Development Report, World Development Indicators. World Bank Group, Washington, D.C., 1994.

[9] Data Bridge Market Research. Global structural health monitoring market: Industry trends and forecast to 2030. Technical report, Data Bridge Market Research, 2022. Industry report.

[10] Grand View Research. Structural health monitoring market size, share & trends analysis report by solution (hardware, software & services), by technology, by application, by region, and segment forecasts, 2023 - 2030. Technical report, Grand View Research, 2023. Market research report.

[11] Astute Analytica. Digital twin for buildings market - industry dynamics, market size, and opportunity forecast to 2032. Technical report, Astute Analytica, March 2024. Industry report.

[12] James M. W. Brownjohn, Alessandro De Stefano, You-Lin Xu, Helmut Wenzel, and A. Emin Aktan. Vibration-based monitoring of civil infrastructure: challenges and successes. *Journal of Civil Structural Health Monitoring*, 1(3):79–95, 2011.

[13] Bart Peeters and Guido De Roeck. One year monitoring of the z24-bridge: Environmental influences versus damage events. *Proceedings of SPIE - The International Society for Optical Engineering*, 2, 05 2000.

[14] Filippo Ubertini, Gabriele Comanducci, Nicola Cavalagli, Anna Laura Pisello, Annibale Luigi Materazzi, and Franco Cotana. Environmental effects on natural frequencies of the san pietro bell tower in perugia, italy, and their removal for structural performance assessment. *Mechanical Systems and Signal Processing*, 82:307–322, 2017.

[15] A.K. Pandey, M. Biswas, and M.M. Samman. Damage detection from changes in curvature mode shapes. *Journal of Sound and Vibration*, 145(2):321 – 332, 1991. Cited by: 2042.

[16] Dimitrios Anastasopoulos, Guido De Roeck, and Edwin P.B. Reynders. Influence of damage versus temperature on modal strains and neutral axis positions of beam-like structures. *Mechanical Systems and Signal Processing*, 134:106311, 2019.

[17] Dimitrios Anastasopoulos, Guido De Roeck, and Edwin P.B. Reynders. One-year operational modal analysis of a steel bridge from high-resolution macrostrain monitoring: Influence of temperature vs. retrofitting. *Mechanical Systems and Signal Processing*, 161:107951, 2021.

[18] Sahar Hassani and Ulrike Dackermann. A systematic review of optimization algorithms for structural health monitoring and optimal sensor placement. *Sensors*, 23(6), 2023.

[19] Vahidreza Gharehbaghi, Ehsan Farsangi, Mohammad Noori, Tony Yang, Shaofan Li, Andy Nguyen, Christian Málaga-Chuquitaype, Paolo Gardoni, and Seyedali Mirjalili. A critical review on structural health monitoring: Definitions, methods, and perspectives. *Archives of Computational Methods in Engineering*, 29, 10 2021.

[20] Dimitrios Anastasopoulos, Edwin Reynders, and Guido De Roeck. Structural health monitoring based on operational modal analysis from long gauge dynamic strain measurements, 2020. Doctoral Thesis.

[21] A. Deraemaeker, E. Reynders, G. De Roeck, and J. Kullaa. Vibration-based structural health monitoring using output-only measurements under changing environment. *Mechanical Systems and Signal Processing*, 22(1):34–56, 2008.

[22] Bart Peeters, J. Maeck, and Guido De Roeck. Vibration-based damage detection in civil engineering: Excitation sources and temperature effects. *Smart Materials and Structures*, 10:518, 06 2001.

[23] Charles Farrar, S. Doebling, Phillip Cornwell, and Erik Straser. Variability of modal parameters measured on the alamosa canyon bridge. *Proceedings of International Modal Analysis Conference*, 1, 01 1997.

[24] Dimitrios Anastasopoulos and Edwin P.B. Reynders. Modal strain monitoring of the old nieuwebrugstraat bridge: Local damage versus temperature effects. *Engineering Structures*, 296:116854, 2023.

[25] Yong Xia, Bo Chen, Shun Weng, Yi-Qing Ni, and You-Lin Xu. Temperature effect on vibration properties of civil structures: A literature review and case studies. *Journal of Civil Structural Health Monitoring*, 2, 05 2012.

[26] Edwin Reynders, Guido De Roeck, Pelin Bakir, and Claude Sauvage. Damage identification on the tilff bridge by vibration monitoring using optical fiber strain sensors. *Journal of Engineering Mechanics*, 133:185–193, 02 2007.

[27] Fabio Marques Dos Santos and Bart Peeters. On the use of strain sensor technologies for strain modal analysis: Case studies in aeronautical applications. *Review of Scientific Instruments*, 87(10):102506, October 2016.

[28] Xue-Yang Pei, Ting-Hua Yi, and Hong-Nan Li. Dual-type sensor placement optimization by fully utilizing structural modal information. *Advances in Structural Engineering*, 22:136943321879915, 09 2018.

[29] Muammer Ozbek and Daniel Rixen. Operational modal analysis of a 2.5mw wind turbine using optical measurement techniques and strain gauges. *Wind Energy*, 04 2013.

[30] Annibale Luigi Materazzi, Filippo Ubertini, and Antonella D'Alessandro. Carbon nanotube cement-based transducers for dynamic sensing of strain. *Cement and Concrete Composites*, 37:2–11, 2013.

[31] Althen Sensors. Tf-series strain gauges for surface temperature measurement, 2024. Accessed: 2024-09-05.

[32] Jun Cong, Xianmin Zhang, Kangsheng Chen, and Jian Xu. Fiber optic bragg grating sensor based on hydrogels for measuring salinity. *Sensors and Actuators B: Chemical*, 87(3):487–490, 2002.

[33] Kenichi Soga and Linqing Luo. Distributed fiber optics sensors for civil engineering infrastructure sensing. *Journal of Structural Integrity and Maintenance*, 3:1–21, 01 2018.

[34] Wieslaw Ostachowicz, Rohan Soman, and Pawel Malinowski. Optimization of sensor placement for structural health monitoring: A review. *Structural health monitoring*, 18(3):963–988, 2019.

[35] Pablo Pachón, María Infantes, Margarita Cámara, Víctor Compán, Enrique García-Macías, Michael I. Friswell, and Rafael Castro-Triguero. Evaluation of optimal sensor placement algorithms for the structural health monitoring of architectural heritage. application to the monastery of san jerónimo de buenavista (seville, spain). *Engineering Structures*, 202:109843, 2020.

[36] M. Salama, T. Rose, and J. Garba. Optimal placement of excitations and sensors for verification of large dynamical systems. In *Proceedings of the 28th Structures, Structural Dynamics and Materials Conference*, Monterey, CA, USA, April 6–8 1987. AIAA. AIAA PAPER 87-0782.

[37] Gene H. Golub and Charles F. Van Loan. *Matrix Computations*. Johns Hopkins University Press, Baltimore, MD, USA, 4th edition, 2013.

[38] Daniel Kammer. Sensor placement for on-orbit modal identification and correlation of large space structures. *Journal of Guidance, Control, and Dynamics*, 14:251 – 259, 06 1991.

[39] Costas Papadimitriou, James L Beck, and Siu-Kui Au. Entropy-based optimal sensor location for structural model updating. *Journal of Vibration and Control*, 6(5):781–800, 2000.

[40] Ying Wang, Yue Chen, Yuhan Yao, and Jinping Ou. Advancements in optimal sensor placement for enhanced structural health monitoring: Current insights and future prospects. *Buildings*, 13:3129, 12 2023.

[41] T.H. Loutas and A. Bourikas. Strain sensors optimal placement for vibration-based structural health monitoring. the effect of damage on the initially optimal configuration. *Journal of Sound and Vibration*, 410:217–230, 2017.

[42] Jinzhu Zhou, Zhiheng Cai, Pengbing Zhao, and Baofu Tang. Efficient sensor placement optimization for shape deformation sensing of antenna structures with fiber bragg grating strain sensors. *Sensors*, 18(8), 2018.

[43] G Cazzulani, M Chieppi, A Colombo, and P Pennacchi. Optimal sensor placement for continuous optical fiber sensors. In *Sensors and Smart Structures Technologies for Civil, Mechanical, and Aerospace Systems 2018*, volume 10598, pages 970–981. SPIE, 2018.

[44] G Cazzulani, A Silva, and P Pennacchi. Optimization of continuous sensor placement for modal analysis: Application to an optical backscatter reflectometry strain sensor. *Mechanical Systems and Signal Processing*, 150:107242, 2021.

[45] C. Papadimitriou. Optimal sensor placement methodology for parametric identification of structural systems. *Journal of Sound and Vibration*, 278(4):923–947, 2004.

[46] Azin Mehrjoo, Mingming Song, Babak Moaveni, Costas Papadimitriou, and Eric Hines. Optimal sensor placement for parameter estimation and virtual sensing of strains on an offshore wind turbine considering sensor installation cost. *Mechanical Systems and Signal Processing*, 169:108787, 2022.

[47] Zifan Zhang, Chang Peng, Guangjun Wang, Zengye Ju, and Long Ma. Optimal sensor placement for strain sensing of a beam of high-speed emu. *Journal of Sound and Vibration*, 542:117359, 2023.

[48] JungHyun Kyung and Hee-Chang Eun. An optimal strain gauge layout design for the measurement of truss structures. *Sensors*, 23(5), 2023.

[49] XH Zhang, Songye Zhu, You Lin Xu, and XJ Homg. Integrated optimal placement of displacement transducers and strain gauges for better estimation of structural response. *International journal of structural stability and dynamics*, 11(03):581–602, 2011.

[50] Songye Zhu, Xiao-Hua Zhang, You-Lin Xu, and Sheng Zhan. Multi-type sensor placement for multi-scale response reconstruction. *Advances in Structural Engineering*, 16(10):1779–1797, 2013.

[51] Chengyin Liu, Zhaoshuo Jiang, Yi Gong, and Yongfeng Xiao. A two-stage optimal sensor placement method for multi-type structural response reconstruction. *Measurement Science and Technology*, 32(3):035114, 2020.

[52] Rune Brincker and Carlos E. Ventura. *Classical Dynamics*. John Wiley & Sons, Ltd, 2015.

[53] Edwin Reynders. System identification methods for (operational) modal analysis: Review and comparison. *Archives of Computational Methods in Engineering*, 19(1):51–124, March 2012.

[54] C. Rainieri and Giovanni Fabbrocino. *Operational Modal Analysis of Civil Engineering Structures: An Introduction and Guide for Applications*. 06 2014.

[55] Lennart Ljung. *System Identification: Theory for the User*. Prentice Hall PTR, Upper Saddle River, NJ, USA, 2nd edition, 1999.

[56] Hector Jensen and Costas Papadimitriou. *Bayesian Finite Element Model Updating*, pages 179–227. Springer International Publishing, Cham, 2019.

[57] Enrique Hernández-Montes, María L. Jalón, Rubén Rodríguez-Romero, Juan Chiachío, Víctor Compán-Cardiel, and Luisa María Gil-Martín. Bayesian structural parameter identification from ambient vibration in cultural heritage buildings: The case of the san jerónimo monastery in granada, spain. *Engineering Structures*, 284:115924, 2023.

[58] S. Brooks, A. Gelman, G.L. Jones, and X.-L Meng. *Handbook of Markov Chain Monte Carlo*. 05 2011.

[59] Juan Chiachio-Ruano, Manuel Chiachio-Ruano, and Shankar Sankararaman, editors. *Bayesian Inverse Problems: Fundamentals and Engineering Applications*. CRC Press, Boca Raton, 1st edition, 2021.

[60] N. Metropolis, A. W. Rosenbluth, M. N. Rosenbluth, A. H. Teller, and E. Teller. Equation of state calculations by fast computing machines. *The Journal of Chemical Physics*, 21(6):1087–1092, 1953.

[61] W. K. Hastings. Monte carlo sampling methods using markov chains and their applications, 1971.

[62] National Instruments. Strain gauge measurement – a tutorial. Application Note 078, National Instruments, 1998.

[63] G. O. Roberts, A. Gelman, and W. R. Gilks. Weak convergence and optimal scaling of random walk metropolis algorithms. *The Annals of Applied Probability*, 7(1):110–120, 1997.